Earth's Observed Hemispheric Albedo Symmetry by Cloud Type: Climatology, Trends, and Tests of Cloud Adjustment Hypotheses

Michael Steven Diamond[1], Jake Joseph Gristey[2], and Graham Feingold[3]

[1]CIRES
[2]CIRES/NOAA CSL
[3]CSD, ESRL, NOAA, Boulder

November 21, 2022

Abstract

Earth's Northern and Southern Hemispheres reflect identical amounts of sunlight. How — and whether — this hemispheric albedo symmetry is maintained remains a mystery. We decompose Earth's hemispheric albedo symmetry into components associated with different cloud types as defined by cloud effective pressure and optical thickness. Greater reflection by the surface, clear-sky atmosphere, and high clouds in the Northern Hemisphere is balanced by low and mid clouds (dominated by stratocumulus) in the Southern Hemisphere. Both hemispheres have darkened by ˜0.5-0.8 W/m2/decade due to decreasing low and mid cloud and surface reflection, partially offset by increasing high cloud reflection. Cloud reflection trends largely follow cloud fraction, with the exception of decreasing stratocumulus albedo in both hemispheres. Hypotheses that all-sky symmetry is maintained despite clear-sky changes via adjustments in high clouds within the Intertropical Convergence Zone or in low and mid clouds in the Southern Ocean are not supported at interannual or decadal timescales.

Earth's Observed Hemispheric Albedo Symmetry by Cloud Type: Climatology, Trends, and Tests of Cloud Adjustment Hypotheses

M. S. Diamond[1,2], J. J. Gristey[1,2,3], and G. Feingold[2]

[1]Cooperative Institute for Research in Environmental Sciences, University of Colorado, Boulder, CO, USA.

[2]NOAA Chemical Sciences Laboratory, Boulder, CO, USA.

[3]Laboratory for Atmospheric and Space Physics, University of Colorado, Boulder, CO, USA.

Corresponding author: Michael Diamond (michael.diamond@noaa.gov)

Key Points:

- Greater reflection from Northern Hemisphere clear-skies and high clouds is balanced by Southern Hemisphere low and mid clouds.
- Both hemispheres show significant darkening trends driven by low and mid clouds and the surface, partially counteracted by high clouds.
- Shifts in tropical high clouds or extratropical low and mid clouds do not compensate clear-sky changes at monthly to decadal timescales.

Abstract

Earth's Northern and Southern Hemispheres reflect identical amounts of sunlight. How — and whether — this hemispheric albedo symmetry is maintained remains a mystery. We decompose Earth's hemispheric albedo symmetry into components associated with different cloud types as defined by cloud effective pressure and optical thickness. Greater reflection by the surface, clear-sky atmosphere, and high clouds in the Northern Hemisphere is balanced by low and mid clouds (dominated by stratocumulus) in the Southern Hemisphere. Both hemispheres have darkened by ~0.5-0.8 W/m^2/decade due to decreasing low and mid cloud and surface reflection, partially offset by increasing high cloud reflection. Cloud reflection trends largely follow cloud fraction, with the exception of decreasing stratocumulus albedo in both hemispheres. Hypotheses that all-sky symmetry is maintained despite clear-sky changes via adjustments in high clouds within the Intertropical Convergence Zone or in low and mid clouds in the Southern Ocean are not supported at interannual or decadal timescales.

Plain Language Summary

Mysteriously, the Northern and Southern Hemispheres reflect the same amount of sunlight as each other, but scientists are not yet sure why or even whether this phenomenon is sustained by the Earth system. The Northern Hemisphere is brighter in clear skies because it contains more pollution particles in the atmosphere and has more land area, whereas the Southern Hemisphere is cloudier. We break down this cloudiness contrast into components related to different cloud types defined by cloud height and thickness. Tropical high-altitude clouds increase reflection preferentially in the Northern Hemisphere but are overcompensated by low- and mid-level clouds in the Southern Hemisphere, especially in the subtropics and midlatitudes. Both hemispheres have darkened over the past two decades at similar rates, but there is no single primary driver of the trends in either hemisphere. Cloud trends are mostly driven by changes in how often clouds occur rather than how bright the clouds are. An important exception is the darkening trend due to the decreasing brightness of low-altitude stratocumulus clouds. We test two hypotheses for how clouds may adjust to compensate for clear-sky differences between the hemispheres but do not find support for either.

1 Introduction

For over half a century, satellite observations have shown that Earth's Northern and Southern Hemispheres (NH and SH, respectively) reflect identical amounts of sunlight to within observational uncertainty (Datseris & Stevens, 2021; Jönsson & Bender, 2021; Ramanathan, 1987; Stephens et al., 2015; Voigt, Stevens, Bader, & Mauritsen, 2013; Vonder Haar & Suomi, 1971). Why this is true — and whether this hemispheric albedo symmetry is physically maintained — has remained a mystery. State-of-the-art coupled climate models do not systematically simulate symmetric hemispheric reflection (Jönsson & Bender, 2021; Stephens et al., 2015; Voigt et al., 2013). A general energy balance argument for the shortwave symmetry is unsatisfactory: emitted longwave radiation is not symmetric, with hemispheric differences in net radiation balanced by net interhemispheric energy transport by the ocean and atmosphere (Stephens et al., 2016).

A further complication is that the hemispheres are markedly asymmetric in their clear-sky reflection, with greater natural and anthropogenic aerosol loadings and land surface coverage in the NH only partly counteracted by greater reflection from the SH poles (Diamond, Gristey, Kay, & Feingold, 2022). Greater SH cloudiness (both in terms of albedo and cloud fraction), especially in the extratropics, accounts for the observed all-sky symmetry (Bender, Engström, Wood, & Charlson, 2017; Datseris & Stevens, 2021; Jönsson & Bender, 2021). Leading hypotheses for how all-sky symmetry may be maintained involve shifts in the Intertropical Convergence Zone (ITCZ), which would implicate tropical high-altitude clouds (Voigt, Stevens, Bader, & Mauritsen, 2014), or changes in Southern Ocean low- and mid-level cloudiness (Datseris & Stevens, 2021). Observational evidence for either hypothesis is currently lacking, and other cloud adjustment mechanisms (or the lack thereof) are possible.

Previous work on the hemispheric asymmetry in cloudiness has mostly treated the "cloudy sky" as a single entity, without separating the influence of different cloud types. An exception is L'Ecuyer et al. (2019), who analyzed hemispheric differences in cloud radiative effect from cloud types identified via active satellite remote sensing. Their combined lidar-radar data are only available over a four year period, however (L'Ecuyer, Hang, Matus, & Wang, 2019). Here, we utilize the Clouds and the Earth's Radiant Energy System (CERES) Flux By Cloud Type (FBCT) passive satellite remote sensing product (Sun et al., 2022) to: 1) analyze how different cloud types contribute to Earth's hemispheric albedo symmetry in a climatological sense; 2) explore how these contributions have changed over the approximately two decade CERES record; and 3) test the leading hypotheses for cloud adjustment mechanisms that maintain all-sky albedo symmetry in the face of clear-sky albedo changes.

2 Methods

2.1 Clouds and the Earth's Radiant Energy System Data

CERES instruments flying on both the Terra and Aqua satellites measure top-of-atmosphere (TOA) shortwave (0.3-5 µm), window (8-12 µm), and total broadband (0.3-200 µm) radiation (Loeb, Doelling, et al., 2018; Wielicki et al., 1996). Here we focus only on the shortwave. The CERES FBCT Edition 4A product uses information from the Moderate Resolution Imaging Spectroradiometer (MODIS) to partition CERES irradiances into 42 bins of cloud effective pressure and optical thickness (Sun et al., 2022). We condense the seven pressure and six optical thickness bins available in CERES FBCT into 9 cloud types (see supporting information Figure S1): low, thin cumulus (Cu); low, medium-thick stratocumulus (Sc); low, thick stratus (St); mid, thin altocumulus (Ac); mid, medium-thick altostratus (As); mid, thick nimbostratus (Ns); high, thin cirrus (Ci); high, medium-thick cirrostratus (Cs); and high, thick cumulonimbus (Cb). Low clouds are defined as having cloud effective pressures greater than 680 hPa and high clouds as less than 440 hPa; thin clouds are defined as having shortwave optical thicknesses less than 3.6 and thick clouds as greater than 23. The cloud type bins are identical to those used in the CERES CldTypHist product and follow those associated with the International Satellite Cloud Climatology Project (Rossow & Schiffer, 1991). We use monthly-average FBCT data at 1° x 1° resolution from the start of the combined Terra-Aqua record in July 2002 up to December 2021.

In addition to CERES FBCT, we also use data from the Synoptic (SYN1deg) Edition 4A product (Doelling et al., 2013; Rutan et al., 2015) to calculate surface albedo and atmospheric transmissivity and the Energy Balanced and Filled (EBAF) Edition 4.1 products (Kato et al., 2018; Loeb, Doelling, et al., 2018) for comparison to previous literature and to check that trends are consistent between datasets. Importantly, CERES FBCT, SYN1deg, and EBAF are not internally consistent in terms of total TOA radiation, especially as SYN1deg incorporates geostationary data to create a more complete diurnal cycle and EBAF is adjusted within observational uncertainty to match observed ocean heat uptake (Johnson, Lyman, & Loeb, 2016; Loeb et al., 2009). Note that the FBCT product applies a diurnal albedo model to obtain daily-averaged fluxes that account for changes in solar geometry while assuming that cloud properties are invariant throughout the day, fixed at the time of the CERES overpass. However, the TOA shortwave flux is known to exhibit diurnal variability associated with cloud evolution (Doelling et al., 2013; Gristey et al., 2018; Rutan, Smith, & Wong, 2014). We therefore only use relative measures like albedo and transmissivity rather than absolute values like reflection when comparing data or applying values calculated in one dataset to another, as we do in Section 2.3.

2.2 Decomposition of Radiative Fluxes into Surface and Atmospheric Components

Top-of-atmosphere (TOA) fluxes are decomposed into atmospheric and surface components following the methodology of Donohoe & Battisti (2011), hereafter DB11:

$$R = R_{\text{atm}} + R_{\text{sfc}} = S\alpha_{\text{atm}} + S\alpha_{\text{sfc}}\frac{\mathcal{T}^2}{(1-\alpha_{\text{atm}}\alpha_{\text{sfc}})}, \qquad (1)$$

where R, R_{atm}, and R_{sfc} are the reflected shortwave flux at TOA and its atmospheric and surface components, respectively; S is the incoming solar flux; α_{atm} and α_{sfc} are the atmospheric and surface albedos, respectively; and $\mathcal{T}$ is the atmospheric transmissivity.

Similar equations were derived in Stephens et al. (2015), hereafter S+15, and have been used extensively since (Datseris & Stevens, 2021; Jönsson & Bender, 2021; Stephens et al., 2022). Figures S2 and S3 compare the clear-sky atmospheric and surface breakdown in the CERES EBAF product using Equation 1 (data from Diamond et al., 2022, following DB11) and using the S+15 equations globally and for polar latitudes, respectively. Although they perform similarly overall, the S+15 equations show greater atmospheric reflection, particularly near the poles (Fig. S2). Especially during local polar spring (Fig. S3a,d), variations in surface upwelling radiation drive top-of-atmosphere reflection variability. This variability manifests in the surface component using the DB11 equations but in the atmospheric component using S+15, suggesting DB11 performs more realistically near the poles. Better understanding under what conditions either set of equations may be preferred would be a useful avenue for future work given the relevance not just to the study of hemispheric albedo symmetry and trends (Stephens et al., 2022), but also to sea ice-albedo feedbacks (Donohoe, Blanchard-Wrigglesworth, Schweiger, & Rasch, 2020).

2.3 Transmissivity

As neither CERES FBCT nor the other Single Scanner Footprint products currently provide computed monthly gridded surface fluxes, we use the SYN1deg product to calculate surface albedo (ratio of upwelling to downwelling shortwave radiation at the surface) and transmissivity (ratio of downwelling radiation at surface to incoming solar radiation). Although this provides us with all-sky and clear-sky transmissivity values, we also need overcast (cloudy-sky) values by cloud type to separate surface and atmospheric contributions when each cloud type is present. We use an ordinary least squares multiple linear regression to estimate transmissivity (first transformed using a logit function to ensure values remain between 0 and 1) as a function of cloud fraction for each of the nine cloud types (C_i), the cosine of solar zenith angle (μ_0), and surface elevation (z_{sfc}):

$$\text{logit}(\hat{\mathcal{T}}) = \widehat{a_0} + \sum_{i=1}^{9} \widehat{\beta_i} C_i + \widehat{\beta_\mu} \mu_0 + \widehat{\beta_z} z_{\text{sfc}}, \quad (2)$$

where the hat accents refer to estimated values, a_0 is the intercept, and each β is a regression coefficient. Figure S4 shows the correspondence between the regressed and SYN1deg computed transmissivities. Overall, the values agree quite well, with a Pearson's correlation coefficient of 0.88 ($p \ll 0.01$) and a clustering of values along the 1:1 line.

The overcast transmissivity when each cloud type is present is calculated using Equation (2) by setting C for the cloud type in question to 1 and all others to 0. Unless otherwise specified, "surface" values refer to the clear-sky surface plus the surface contribution under each cloud type and reflection by a particular cloud type refers to the atmospheric contribution only.

2.4 Trend Analysis

To calculate trends, we first decompose the reflection data into monthly means and deseasonalized anomalies:

$$R(y, m) = \bar{R}(m) + R'(y, m), \quad (3)$$

where y is the year and m the month and the overbars refer to the monthly climatologies and primes to the deseasonalized anomalies. The climatology is defined as the mean value from July 2005 to June 2015, inclusive, and anomalies are defined relative to this mean. Temporal averaging accounts for different month lengths and leap years (Datseris & Stevens, 2021; Diamond et al., 2022). Trends over the CERES record are calculated using the deseasonalized anomalies independently for each grid point and for various global, hemispheric, and regional averages. Spatial averaging accounts for Earth's oblate spheroidal geometry (Diamond et al., 2022). Climatologies, anomalies, and trends are calculated for cloud fraction and overcast albedo in the same manner.

Time series are assumed to be characterized by red noise and uncertainties are calculated accordingly (Bretherton, Widmann, Dymnikov, Wallace, & Bladé, 1999; Santer et al., 2000). For error propagation when manipulating trend values, errors are assumed to be independent. Radiometric uncertainties are neglected as random spatiotemporally averaged errors become negligibly small compared with errors due to red noise statistics (Diamond et al., 2022; Donohoe & Battisti, 2011), although (currently unquantified) systematic errors by surface or cloud type could be of greater concern. For example, there are some anomalies in the Cu fields in the north tropical Atlantic associated with the MODIS cloud retrieval dust mask that may affect the partitioning between clear-sky and thin-Cu reflection.

3 Results

3.1 Climatology

Figure 1 shows the climatology of total all-sky reflection for each hemisphere and its components related to the all-sky surface contribution (sfc), clear-sky atmosphere (atm), and each cloud type. Reflection asymmetries (ΔR) are defined as the NH-SH difference (i.e., positive values indicate greater NH reflection). Global maps of the total all-sky (Fig. S5), surface (Fig. S6), clear-sky atmosphere (Fig. S7), and cloud type (Fig. S8-16) climatologies are provided in the supporting information.

Overall, the NH and SH reflect identical amounts of sunlight because greater NH contributions from the surface, clear-sky atmosphere, and high-altitude clouds are perfectly balanced by greater SH contributions from low- and mid-level clouds (Fig. 1a). Stratocumulus clouds play a disproportionate role in the balance, with a SH-favoring contribution nearly twice as large as any other single component. Zonally (Fig. 1b-c), in the deep tropics, the NH high cloud advantage is largely associated with the northward mean location of the ITCZ; in the subtropics and midlatitudes, greater NH land and clear-sky atmospheric components largely balance SH stratocumulus clouds; and toward the poles, the SH surface dominates (associated with the extremely bright Antarctic ice sheets; Diamond et al., 2022).

3.2 Trends

Figure 2 shows trends over the CERES FBCT record for total all-sky reflection and its surface, clear-sky atmosphere, and cloud type components. Total clear-sky trends and their atmospheric and surface components are also shown. Clear-sky reflection values here are calculated as SA_{clr}, SA_{atm}, and SA_{sfc}, where A here refers to the total TOA albedo and the atmospheric and surface contributions to TOA albedo (as distinct from component albedos α), so that they are independent of cloud coverage. Global maps of the trends are provided in Figures S5-16.

In terms of total all-sky reflection, the NH has darkened at a rate of -0.77 ± 0.23 W/m^2/decade (errors represent 95% confidence), closely matched by the SH at -0.53 ± 0.27 W/m^2/decade, resulting in a global darkening of -0.65 ± 0.16 W/m^2/decade. The hemispheric contrast has been moving toward favoring the SH at a rate of -0.24 ± 0.34 W/m^2/decade, which is statistically indistinguishable from zero but also similar in magnitude to the total clear-sky asymmetry trend of -0.33 ± 0.34 W/m^2/decade (which is significant at 90% confidence but just shy at 95%). The global clear-sky trend of -0.34 ± 0.14 W/m^2/decade is dominated by nearly equal NH and SH surface reflection declines whereas the asymmetry trend is dominated by declining NH atmospheric reflection associated with a reduction of anthropogenic aerosol over eastern North America, Europe, and eastern Asia (Fig. S7d; (Quaas et al., 2022; Raghuraman, Paynter, & Ramaswamy, 2021; Stephens et al., 2022).

Neither hemisphere has a single dominant driver for the total all-sky darkening (Fig. 2, Table S1). Globally, low clouds (led by Sc) are the largest contributor to the darkening trend, followed by nearly equal mid cloud and surface contributions. The clear-sky atmospheric trend is negligible and high clouds (led by Cs) provide a small countervailing positive trend. In the NH, darkening is driven most by low clouds (primarily Sc) followed by the surface and mid clouds with a small and uncertain clear-sky atmosphere contribution and is partially offset by high clouds (primarily Cs). In the SH, darkening is driven by low (primarily Cu) and mid clouds (primarily As) about equally, followed by the surface, with a negligible high cloud contribution (due to strong cancellation between positive Cs and negative Cb trends) and a small countervailing clear-sky atmospheric trend.

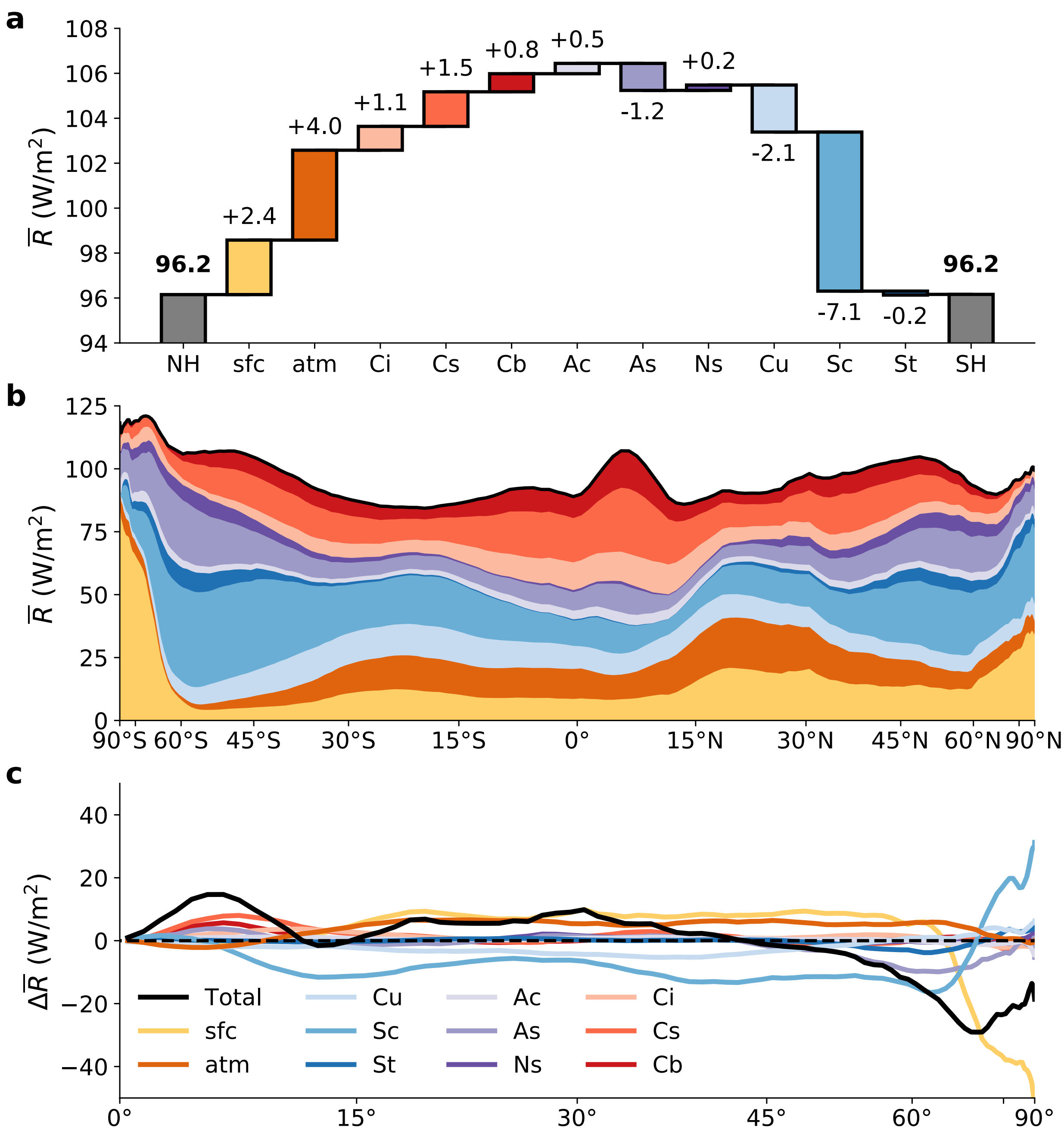

Figure 1. Climatology (July 2005 to June 2015) of Earth's hemispheric albedo symmetry decomposed into all-sky surface, clear-sky atmospheric, and cloud type components. (a) Waterfall chart showing the hemispheric compensation between the all-sky surface (sfc), clear-sky atmosphere (atm), and different cloud types (Ci to St). Greater NH reflection is indicated by positive contributions and greater SH reflection by negative contributions. (b) Zonal average surface, clear-sky atmosphere, and cloud-type contributions to the total reflection. (c) Zonal hemispheric differences (NH-SH) in total reflection and its surface, clear-sky atmosphere, and cloud type components.

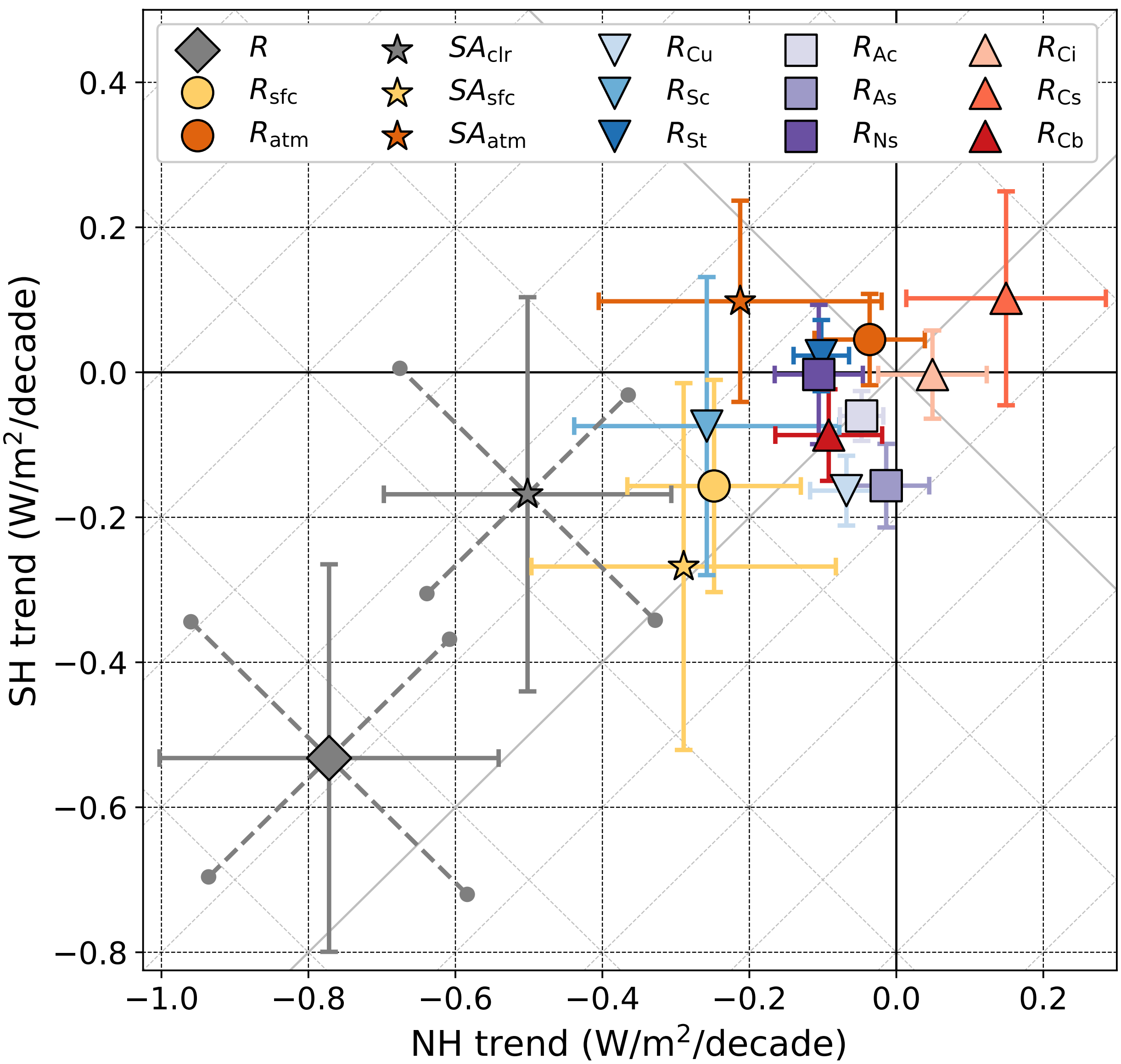

Figure 2. Northern and Southern Hemispheric trends in all-sky and clear-sky reflection and their surface and atmospheric components. Error bars represent 95% confidence. Gray diagonal lines indicate global (top left to bottom right) and hemispheric difference (bottom left to top right) trends in 0.2 W/m^2/decade increments. Dashed, diagonal error bars for the global and hemispheric difference trends are provided for total all-sky and clear-sky reflection.

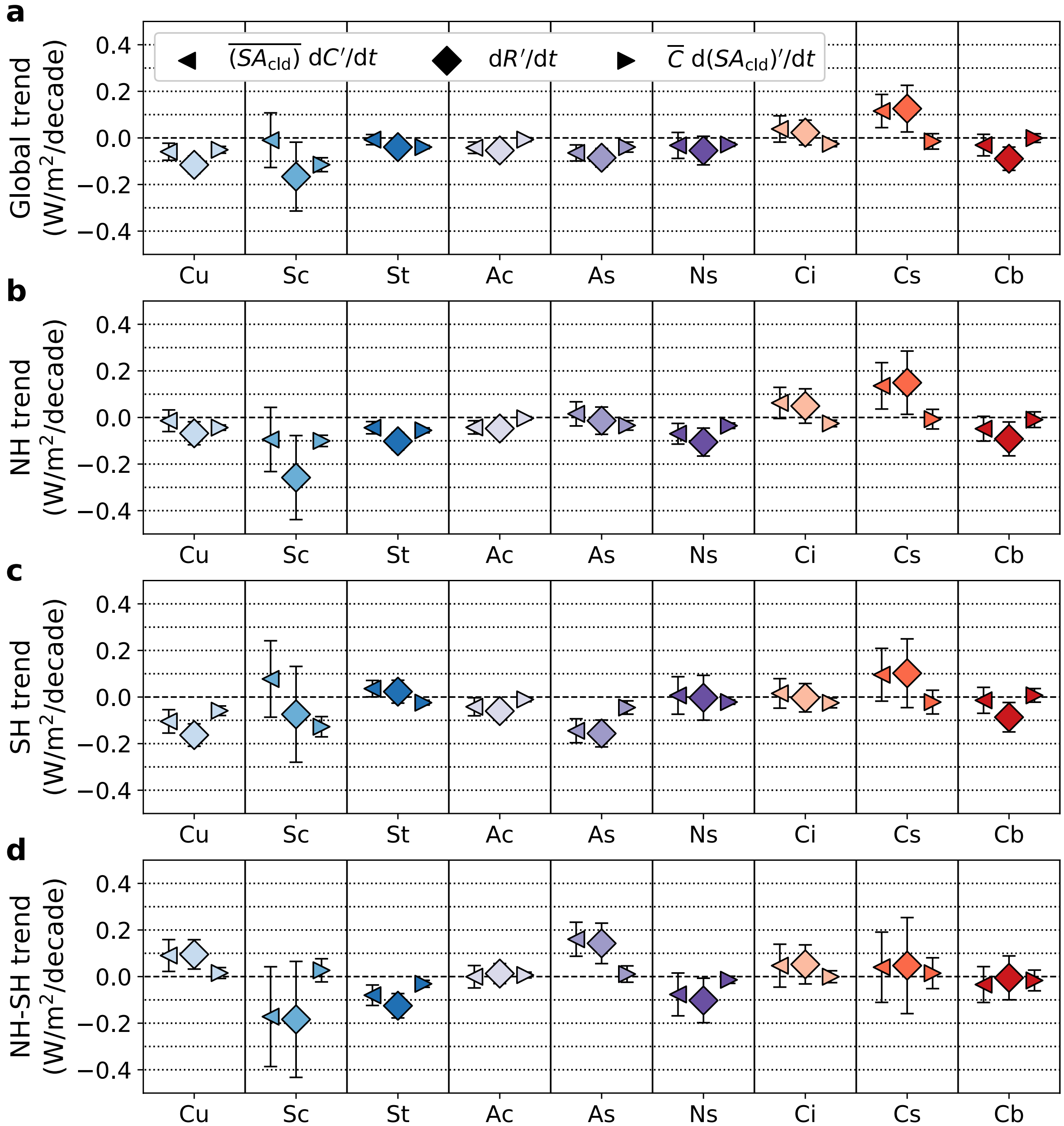

Figure 3. Trends in reflection for each cloud type. Total reflection changes (diamond markers) are broken down into components related to changing cloud fraction (left-facing triangles) and cloud albedo (right-facing triangles) globally (a) and for the NH (b), SH (c), and the NH-SH difference (d). Error bars represent 95% confidence.

Figure 3 shows the cloud trends broken into components related to the linear contributions from changes in cloud fraction versus changes in cloud albedo, SA_{cld}, where A_{cld} is the TOA albedo in overcast conditions. A caveat here is that a shift of clouds toward lower latitudes or summer months will be recorded as increasing brightness even if the cloud optical thickness remains constant. Discrepancies between the sum of the cloud fraction and albedo-related trends and the overall cloud reflection trend are due to non-linearities, which are generally small compared to the uncertainty, with the exception of Cb.

Cloud reflection trends in general follow changes in cloud fraction rather than cloud albedo (Fig. 3, Figs. S8-16b-c). The most important exception to this pattern is the global decline in Sc reflection, which is driven primarily by cloud dimming due to opposing cloud fraction trends in the NH and SH. The (uncertain) strengthening of the SH cloudiness advantage is, however, driven by Sc cloud fraction trends. Spatial trends (Fig. S9b-c) clearly show Sc declines in the northeast Pacific (Andersen, Cermak, Zipfel, & Myers, 2022; Loeb, Thorsen, Norris, Wang, & Su, 2018; Stephens et al., 2022), but also show substantial trends of decreasing cloud fraction in the southeast Atlantic and increasing cloud fraction in the southeast Pacific and northeast Atlantic. Sc albedo has been decreasing in almost all regions, with particularly strong trends off the western coasts of North America and southern Africa (Fig. S9d).

Cs are the only cloud type to show a significant brightening trend. One possible explanation is that the Cs brightening and Cb darkening are linked — some high clouds are dimming such that they are moving from the Cb to the Cs classification. The spatial patterns of the Cs and Cb trends do not support this hypothesis, however, as both clouds generally are brightening and darkening in the same regions while Cs have an additional diffuse brightening trend in the poleward storm tracks (Figs. S15-16b). Together, the increasing Sc cloud in the tropical east Pacific and shift of high clouds further toward the Maritime Continent are consistent with a decadal La Niña-like trend in sea surface temperatures that has been implicated in driving anomalously negative cloud feedbacks (Zhou, Zelinka, & Klein, 2016). Trends over the CERES record capture decadal climate variability in addition to more secular changes due to changing aerosol and increasing greenhouse gases.

3.3 Testing Cloud Adjustment Hypotheses

The core mystery of Earth's hemispheric albedo symmetry is how and whether clouds adjust to compensate for the large differences in Earth's clear-sky albedo. As the strength of the clear-sky hemispheric asymmetry is transient due to its dependence on aerosol and ice cover (Diamond et al., 2022), these adjustments should operate on at least decadal timescales given that all-sky symmetry was first observed in the 1960s and has persisted throughout the CERES record (Stephens et al., 2015; Vonder Haar & Suomi, 1971). Although anthropogenic aerosol forcing has been relatively flat from the late 1960s to present due to increases in eastern and southern Asia compensating for decreases in Europe and North America (Smith et al., 2021), Arctic and Antarctic sea ice trends were strongly contrasting until relatively recently (Meier, Stroeve, & Fetterer, 2007; Parkinson & Cavalieri, 2012). Here, we test whether variability in the clear-sky asymmetry is balanced by changes in tropical high clouds via shifts in the ITCZ (Voigt et al., 2014) or by changes in extratropical low and mid clouds (Datseris & Stevens, 2021) on monthly to decadal timescales. Regional reflection values are weighted based on their influence on global values (e.g., a tropical trend of 2 W/m^2/decade corresponds to a global trend of 1 W/m^2/decade).

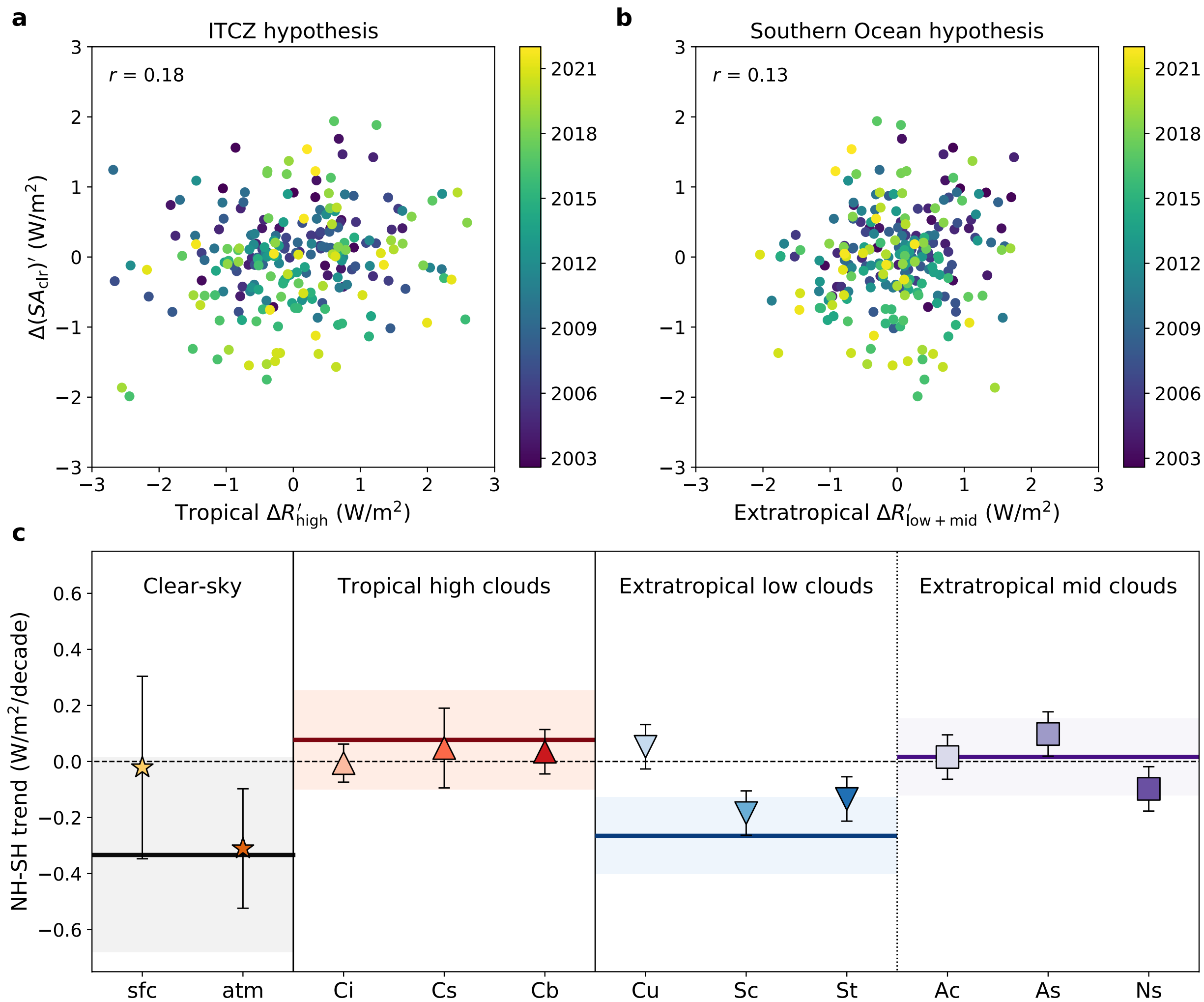

Figure 4. Testing hypotheses that shifts in tropical high-altitude clouds or in extratropical low- and mid-level clouds compensate for changes in clear-sky hemispheric albedo asymmetry at monthly to decadal timescales. (a) Correlation between deseasonalized monthly anomalies in clear-sky and tropical (0-30°) high cloud (Ci+Cs+Cb) reflection asymmetries (NH-SH). Shading indicates time. (b) As in (a), but for extratropical (30-90°) low and mid clouds (Cu+Sc+St+Ac+As+Ns). (c) NH-SH trends for the clear-sky, tropical high clouds, and extratropical low and mid clouds. Total trends are shown as horizontal lines (means) and shading (95% confidence) and components as markers (means) and error bars (95% confidence).

For cloud adjustments to balance clear-sky variability at monthly timescales, we would expect a strong negative correlation between the deseasonalized anomalies of the clear-sky asymmetry and the tropical high cloud or extratropical low and mid cloud asymmetries. Figure 4a&b shows the correlations in the CERES FBCT record. Both correlations are small and positive, suggesting that neither hypothesis is supported at the monthly timescale. Correlations do not appreciably improve when testing various lag relationships (Figure S17). This result is consistent with Datseris & Stevens (2021), who found that residuals in NH and SH reflection after accounting for seasonal cycles are indistinguishable from noise and uncorrelated across the hemispheres at intra- to interannual timescales yet had extremely similar decadal trends.

For cloud adjustments to balance clear-sky changes at decadal timescales, we would expect the trends to be similar in magnitude but opposite in sign. Figure 4c shows the global clear-sky, tropical high cloud, and extratropical low and mid cloud asymmetry trends and their components. The tropical high cloud asymmetry trend is opposite in sign to that of the clear-sky asymmetry but much smaller in magnitude whereas the combined extratropical low and mid cloud asymmetry trends are similar in magnitude to the clear-sky trend but of the same sign. Neither hypothesis is therefore supported at the decadal timescale either.

Our results here do not prove that adjustment mechanisms involving the ITCZ or Southern Ocean clouds do not exist; rather, they show that if such mechanisms exist, they are much subtler than simply compensating for clear-sky changes. Although the clear-sky asymmetry is fundamental for understanding the mean state of Earth's hemispheric albedo symmetry, changes in any single component may be of equal importance in terms of symmetry-maintaining adjustments. Correlations between total all-sky reflection and tropical high cloud and extratropical low and mid cloud (a)symmetry anomalies are also positive, however. At least for the tropical high clouds, this result is consistent with the findings of Jönsson & Bender (2021) that the El Niño-Southern Oscillation dominates monthly variability in the all-sky hemispheric reflection difference.

4 Discussion and Conclusions

The question of why Earth's Northern and Southern Hemispheres reflect identical amounts of sunlight despite having such different clear-sky features is both intrinsically fascinating but also potentially of practical importance for Earth's radiation budget and hydrological cycle if cloud adjustments operate over the next few decades to counteract a projected decline in the clear-sky albedo asymmetry (Diamond et al., 2022). Our contribution is to break down the observed hemispheric symmetry by cloud type using the CERES FluxByCldTyp product. Climatologically, greater NH reflection from the surface, clear-sky atmosphere, and high clouds is balanced by greater SH reflection from low and mid clouds (particularly Sc). Both hemispheres show darkening trends driven by a combination of decreasing low cloud, mid cloud, and surface reflection with small or countervailing contributions from the clear-sky atmosphere and high clouds. Neither shifts in tropical high clouds (Voigt et al., 2014) nor extratropical low and mid clouds (Datseris & Stevens, 2021) compensate changes in clear-sky asymmetry at monthly to decadal timescales.

Our surface and clear-sky atmosphere trend results are qualitatively consistent with recent radiative flux perturbation results (Loeb et al., 2021) but differ dramatically from the findings of Stephens et al. (2022), which show negligible global all-sky and clear-sky surface reflection changes and large darkening from the clear-sky atmosphere. Differences between CERES FBCT/SYN1deg and EBAF cannot explain this discrepancy, but the differences between the surface/atmosphere decomposition methods of DB11 (used here) and S+15 (used in Stephens et al., 2022) may (Figs. S2-3). Our surface trends are driven largely by changes in sea ice (Fig. S6), which the S+15 method may attribute to the atmosphere instead of the surface (Fig. S3).

One limitation of our study is its reliance on passive satellite remote sensing and cloud types defined solely by cloud effective pressure and optical thickness rather than any information about morphology or vertical profiles. Active remote sensing has, e.g., revealed the importance of multilayer clouds (L'Ecuyer et al., 2019) and can provide more physically meaningful distinctions between low cloud types (Cesana, Del Genio, & Chepfer, 2019). Unfortunately, A-train radar and lidar data are limited temporally (~4-year combined record and daytime overpasses at 13:30 local only) and spatially (narrow footprint as compared with the CERES and MODIS swaths). Our cloud types also differ from what a surface observer would pick out via cloud morphology and context. For example, "cirrostratus" often refers to very thin sheets of ice clouds that produce stunning optical phenomena but here refers generically to high-altitude clouds of intermediate optical thickness.

Breaking down Earth's hemispheric albedo symmetry by cloud type can generate important insights; however, the fundamental mystery of how and whether Earth's albedo symmetry is maintained remains unresolved. The trend in total all-sky symmetry is indistinguishable from zero, but also from the clear-sky asymmetry trend. As the clear-sky trend should increasingly favor the SH as anthropogenic aerosol and/or Arctic sea ice coverage decline (Diamond et al., 2022), larger signals will likely be observable in the coming years-to-decades that may reveal robust cloud adjustments or, alternatively, a departure from hemispheric albedo symmetry.

Acknowledgments

M.S.D. acknowledges funding from the CIRES Visiting Fellows Program through the NOAA Cooperative Agreement with CIRES (NA17OAR4320101). J.J.G. also acknowledges funding from the NOAA Cooperative Agreement with CIRES and additionally acknowledges the Libera project under NASA Contract 80LARC20D0006. Both J.J.G. and G.F. acknowledge funding from the NOAA Atmospheric Science for Renewable Energy (ASRE) program. G.F. additionally acknowledges funding from the NOAA Climate Program Office Earth's Radiation Budget initiative (#03-01-07-001).

Open Research Statement

CERES data products are publicly available via the NASA Langley Research Center (https://ceres.larc.nasa.gov/data/); for EBAF, see " EBAF-TOA – Level 3b" and " EBAF – Level 3b" under " Energy Balanced and Filled (EBAF)"; for SYN1deg, see " SYN1deg – Level 3" under "Synoptic TOA and surface fluxes and clouds (SYN)"; and for FBCT, see "FluxByCldTyp – Level 3" under "Single Scanner Footprint (SSF)". Processed data to aid in replicating the analyses in this work are available from the NOAA Chemical Sciences Laboratory's Clouds, Aerosol, & Climate program (https://csl.noaa.gov/groups/csl9/datasets/data/cloud_phys/2022-Diamond-Gristey-Feingold/).

All software used in the data processing and analyses for this paper is publicly available: cartopy (Met Office, 2010-2015) with Natural Earth raster and vector map data and using the Equal Earth projection (Šavrič, Patterson, & Jenny, 2018), matplotlib (Hunter, 2007), numpy (Harris et al., 2020), scipy (Virtanen et al., 2020), and xarray (Hoyer & Hamman, 2017).

References

Andersen, H., Cermak, J., Zipfel, L., & Myers, T. A. (2022). Attribution of Observed Recent Decrease in Low Clouds Over the Northeastern Pacific to Cloud-Controlling Factors. *Geophysical Research Letters, 49*(3). doi:10.1029/2021gl096498

Bender, F. A. M., Engström, A., Wood, R., & Charlson, R. J. (2017). Evaluation of Hemispheric Asymmetries in Marine Cloud Radiative Properties. *Journal of Climate, 30*(11), 4131-4147. doi:10.1175/jcli-d-16-0263.1

Bretherton, C. S., Widmann, M., Dymnikov, V. P., Wallace, J. M., & Bladé, I. (1999). The Effective Number of Spatial Degrees of Freedom of a Time-Varying Field. *Journal of Climate, 12*(7), 1990-2009. doi:10.1175/1520-0442(1999)012<1990:Tenosd>2.0.Co;2

Cesana, G., Del Genio, A. D., & Chepfer, H. (2019). The Cumulus And Stratocumulus CloudSat-CALIPSO Dataset (CASCCAD). *Earth Syst. Sci. Data, 11*(4), 1745-1764. doi:10.5194/essd-11-1745-2019

Datseris, G., & Stevens, B. (2021). Earth's Albedo and Its Symmetry. *AGU Advances, 2*(3). doi:10.1029/2021av000440

Diamond, M., Gristey, J. J., Kay, J. E., & Feingold, G. (2022). On the rise and fall of Earth's strong clear-sky hemispheric albedo asymmetry. *ESSOAr*. doi:10.1002/essoar.10511017.2

Doelling, D. R., Loeb, N. G., Keyes, D. F., Nordeen, M. L., Morstad, D., Nguyen, C., . . . Sun, M. (2013). Geostationary Enhanced Temporal Interpolation for CERES Flux Products. *Journal of Atmospheric and Oceanic Technology, 30*(6), 1072-1090. doi:10.1175/jtech-d-12-00136.1

Donohoe, A., & Battisti, D. S. (2011). Atmospheric and Surface Contributions to Planetary Albedo. *Journal of Climate, 24*(16), 4402-4418. doi:10.1175/2011jcli3946.1

Donohoe, A., Blanchard-Wrigglesworth, E., Schweiger, A., & Rasch, P. J. (2020). The Effect of Atmospheric Transmissivity on Model and Observational Estimates of the Sea Ice Albedo Feedback. *Journal of Climate, 33*(13), 5743-5765. doi:10.1175/jcli-d-19-0674.1

Gristey, J. J., Chiu, J. C., Gurney, R. J., Morcrette, C. J., Hill, P. G., Russell, J. E., & Brindley, H. E. (2018). Insights into the diurnal cycle of global Earth outgoing radiation using a numerical weather prediction model. *Atmos. Chem. Phys., 18*(7), 5129-5145. doi:10.5194/acp-18-5129-2018

Harris, C. R., Millman, K. J., van der Walt, S. J., Gommers, R., Virtanen, P., Cournapeau, D., . . . Oliphant, T. E. (2020). Array programming with NumPy. *Nature, 585*(7825), 357-362. doi:10.1038/s41586-020-2649-2

Hoyer, S., & Hamman, J. J. (2017). xarray: N-D labeled Arrays and Datasets in Python. *Journal of Open Research Software, 5*. doi:10.5334/jors.148

Hunter, J. D. (2007). Matplotlib: A 2D Graphics Environment. *Computing in Science & Engineering, 9*(3), 90-95. doi:10.1109/MCSE.2007.55

Johnson, G. C., Lyman, J. M., & Loeb, N. G. (2016). Improving estimates of Earth's energy imbalance. *Nature Climate Change, 6*(7), 639-640. doi:10.1038/nclimate3043

Jönsson, A., & Bender, F. A. M. (2021). Persistence and variability of Earth's inter-hemispheric albedo symmetry in 19 years of CERES EBAF observations. *Journal of Climate, 35*, 249–268. doi:10.1175/jcli-d-20-0970.1

Kato, S., Rose, F. G., Rutan, D. A., Thorsen, T. J., Loeb, N. G., Doelling, D. R., . . . Ham, S.-H. (2018). Surface Irradiances of Edition 4.0 Clouds and the Earth's Radiant Energy System (CERES) Energy Balanced and Filled (EBAF) Data Product. *Journal of Climate, 31*(11), 4501-4527. doi:10.1175/jcli-d-17-0523.1

L'Ecuyer, T. S., Hang, Y., Matus, A. V., & Wang, Z. (2019). Reassessing the Effect of Cloud Type on Earth's Energy Balance in the Age of Active Spaceborne Observations. Part I: Top of Atmosphere and Surface. *Journal of Climate, 32*(19), 6197-6217. doi:10.1175/jcli-d-18-0753.1

Loeb, N. G., Doelling, D. R., Wang, H., Su, W., Nguyen, C., Corbett, J. G., . . . Kato, S. (2018). Clouds and the Earth's Radiant Energy System (CERES) Energy Balanced and Filled (EBAF) Top-of-Atmosphere (TOA) Edition-4.0 Data Product. *Journal of Climate, 31*(2), 895-918. doi:10.1175/jcli-d-17-0208.1

Loeb, N. G., Johnson, G. C., Thorsen, T. J., Lyman, J. M., Rose, F. G., & Kato, S. (2021). Satellite and Ocean Data Reveal Marked Increase in Earth's Heating Rate. *Geophysical Research Letters, 48*(13). doi:10.1029/2021gl093047

Loeb, N. G., Thorsen, T., Norris, J., Wang, H., & Su, W. (2018). Changes in Earth's Energy Budget during and after the "Pause" in Global Warming: An Observational Perspective. *Climate, 6*(3). doi:10.3390/cli6030062

Loeb, N. G., Wielicki, B. A., Doelling, D. R., Smith, G. L., Keyes, D. F., Kato, S., . . . Wong, T. (2009). Toward Optimal Closure of the Earth's Top-of-Atmosphere Radiation Budget. *Journal of Climate, 22*(3), 748-766. doi:10.1175/2008jcli2637.1

Meier, W. N., Stroeve, J., & Fetterer, F. (2007). Whither Arctic sea ice? A clear signal of decline regionally, seasonally and extending beyond the satellite record. *Annals of Glaciology, 46*, 428-434. doi:10.3189/172756407782871170

Met Office. (2010-2015). Cartopy: a cartographic python library with a matplotlib interface. Exeter, Devon. Retrieved from http://scitools.org.uk/cartopy

Parkinson, C. L., & Cavalieri, D. J. (2012). Antarctic sea ice variability and trends, 1979-2010. *The Cryosphere, 6*(4), 871-880. doi:10.5194/tc-6-871-2012

Quaas, J., Jia, H., Smith, C., Albright, A. L., Aas, W., Bellouin, N., . . . Schulz, M. (2022). Robust evidence for reversal in the aerosol effective climate forcing trend. *Atmos. Chem. Phys. Discuss., 2022*, 1-25. doi:10.5194/acp-2022-295

Raghuraman, S. P., Paynter, D., & Ramaswamy, V. (2021). Anthropogenic forcing and response yield observed positive trend in Earth's energy imbalance. *Nat Commun, 12*(1), 4577. doi:10.1038/s41467-021-24544-4

Ramanathan, V. (1987). The role of earth radiation budget studies in climate and general circulation research. *Journal of Geophysical Research: Atmospheres, 92*(D4), 4075-4095. doi:10.1029/JD092iD04p04075

Rossow, W. B., & Schiffer, R. A. (1991). ISCCP Cloud Data Products. *Bulletin of the American Meteorological Society, 72*(1), 2-20. doi:10.1175/1520-0477(1991)072<0002:Icdp>2.0.Co;2

Rutan, D. A., Kato, S., Doelling, D. R., Rose, F. G., Nguyen, L. T., Caldwell, T. E., & Loeb, N. G. (2015). CERES Synoptic Product: Methodology and Validation of Surface Radiant Flux. *Journal of Atmospheric and Oceanic Technology, 32*(6), 1121-1143. doi:10.1175/jtech-d-14-00165.1

Rutan, D. A., Smith, G. L., & Wong, T. (2014). Diurnal Variations of Albedo Retrieved from Earth Radiation Budget Experiment Measurements. *Journal of Applied Meteorology and Climatology, 53*(12), 2747-2760. doi:10.1175/jamc-d-13-0119.1

Santer, B. D., Wigley, T. M. L., Boyle, J. S., Gaffen, D. J., Hnilo, J. J., Nychka, D., . . . Taylor, K. E. (2000). Statistical significance of trends and trend differences in layer-average atmospheric temperature time series. *Journal of Geophysical Research: Atmospheres, 105*(D6), 7337-7356. doi:10.1029/1999jd901105

Šavrič, B., Patterson, T., & Jenny, B. (2018). The Equal Earth map projection. *International Journal of Geographical Information Science, 33*(3), 454-465. doi:10.1080/13658816.2018.1504949

Smith, C. J., Harris, G. R., Palmer, M. D., Bellouin, N., Collins, W., Myhre, G., . . . Forster, P. M. (2021). Energy Budget Constraints on the Time History of Aerosol Forcing and Climate Sensitivity. *Journal of Geophysical Research: Atmospheres, 126*(13). doi:10.1029/2020jd033622

Stephens, G. L., Hakuba, M. Z., Hawcroft, M., Haywood, J. M., Behrangi, A., Kay, J. E., & Webster, P. J. (2016). The Curious Nature of the Hemispheric Symmetry of the Earth's Water and Energy Balances. *Current Climate Change Reports, 2*(4), 135-147. doi:10.1007/s40641-016-0043-9

Stephens, G. L., Hakuba, M. Z., Kato, S., Gettleman, A., Dufresne, J.-L., Andrews, T., . . . Mauritsen, T. (2022). The changing nature of Earth's reflected sunlight. *Proceedings of the Royal Society A: Mathematical, Physical and Engineering Sciences, 478*(2263). doi:10.1098/rspa.2022.0053

Stephens, G. L., O'Brien, D., Webster, P. J., Pilewski, P., Kato, S., & Li, J.-l. (2015). The albedo of Earth. *Reviews of Geophysics, 53*(1), 141-163. doi:10.1002/2014rg000449

Sun, M., Doelling, D. R., Loeb, N. G., Scott, R. C., Wilkins, J., Nguyen, L. T., & Mlynczak, P. (2022). Clouds and the Earth's Radiant Energy System (CERES) FluxByCldTyp Edition 4 Data Product. *Journal of Atmospheric and Oceanic Technology, 39*(3), 303-318. doi:10.1175/jtech-d-21-0029.1

Virtanen, P., Gommers, R., Oliphant, T. E., Haberland, M., Reddy, T., Cournapeau, D., . . . SciPy, C. (2020). SciPy 1.0: fundamental algorithms for scientific computing in Python. *Nat Methods, 17*(3), 261-272. doi:10.1038/s41592-019-0686-2

Voigt, A., Stevens, B., Bader, J., & Mauritsen, T. (2013). The Observed Hemispheric Symmetry in Reflected Shortwave Irradiance. *Journal of Climate, 26*(2), 468-477. doi:10.1175/jcli-d-12-00132.1

Voigt, A., Stevens, B., Bader, J., & Mauritsen, T. (2014). Compensation of Hemispheric Albedo Asymmetries by Shifts of the ITCZ and Tropical Clouds. *Journal of Climate, 27*(3), 1029-1045. doi:10.1175/jcli-d-13-00205.1

Vonder Haar, T. H., & Suomi, V. E. (1971). Measurements of the Earth's Radiation Budget from Satellites During a Five-Year Period. Part I: Extended Time and Space Means. *Journal of Atmospheric Sciences, 28*(3), 305-314. doi:10.1175/1520-0469(1971)028<0305:Moterb>2.0.Co;2

Wielicki, B. A., Barkstrom, B. R., Harrison, E. F., Lee, R. B., Smith, G. L., & Cooper, J. E. (1996). Clouds and the Earth's Radiant Energy System (CERES): An Earth Observing System Experiment. *Bulletin of the American Meteorological Society, 77*(5), 853-868. doi:10.1175/1520-0477(1996)077<0853:Catere>2.0.Co;2

Zhou, C., Zelinka, M. D., & Klein, S. A. (2016). Impact of decadal cloud variations on the Earth's energy budget. *Nature Geoscience*. doi:10.1038/ngeo2828

Geophysical Research Letters

Supporting Information for

Earth's Observed Hemispheric Albedo Symmetry by Cloud Type: Climatology, Trends, and Tests of Cloud Adjustment Hypotheses

M. S. Diamond[1,2], J. J. Gristey[1,2,3], and G. Feingold[2]

[1]Cooperative Institute for Research in Environmental Sciences, University of Colorado, Boulder, CO, USA.

[2]NOAA Chemical Sciences Laboratory, Boulder, CO, USA.

[3]Laboratory for Atmospheric and Space Physics, University of Colorado, Boulder, CO, USA.

Contents of this file

Introduction

The supporting information document contains figures providing further information about the definitions of the cloud types used in this paper (Figure S1); a comparison of the DB11 and S+15 atmosphere/surface reflection decomposition methods in terms of global climatologies (Figure S2) and time series near the poles (Figure S3); an evaluation of the transmissivity values calculated in Section 2.3 (Figure S4); global maps of reflection climatologies and trends for all-sky and clear-sky reflection and their surface, clear-sky atmospheric, and cloud type components (Figures S5-16, respectively); lagged correlations between clear-sky and tropical high cloud/extratropical low and mid cloud asymmetry anomalies (Figure S17); and a table of global, NH, SH, and NH-SH trends (Table S1).

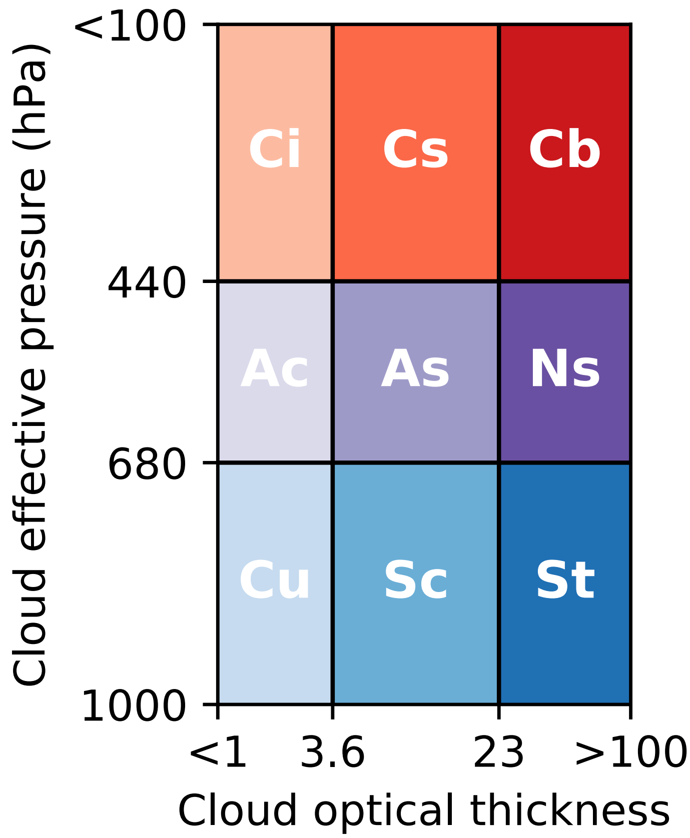

Figure S1. Schematic showing each of the nine cloud types as defined by their cloud effective pressure and cloud optical thickness. Warmer colors indicate higher altitude clouds and darker shades indicate optically thicker clouds.

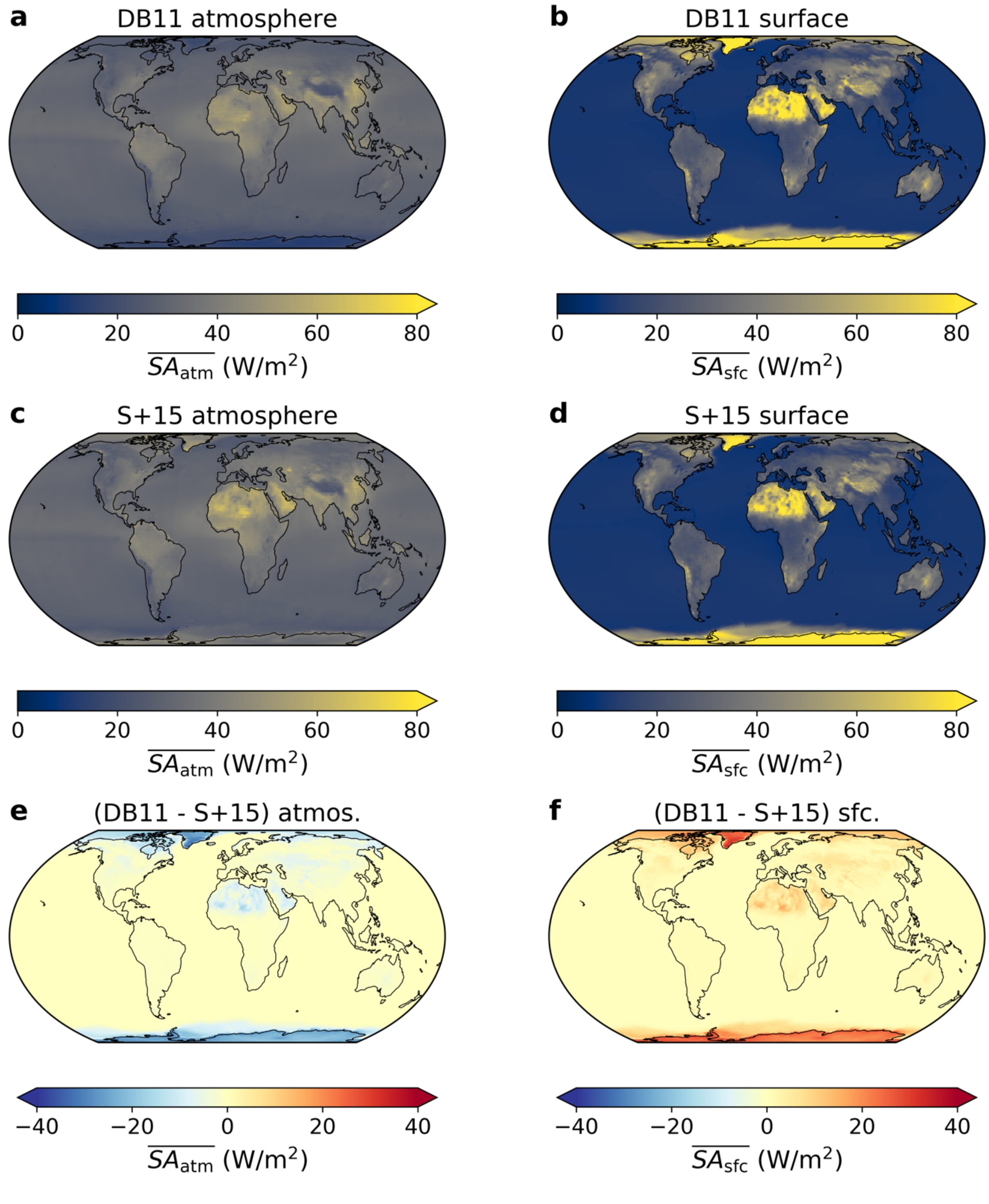

Figure S2. Global differences in atmospheric and surface reflection between the DB11 and S+15 decomposition methods. Climatology (July 2005 to June 2015) of the atmospheric and surface components of TOA reflection for DB11 (a-b), S+15 (c-d), and their difference (e-f) using the CERES EBAF product.

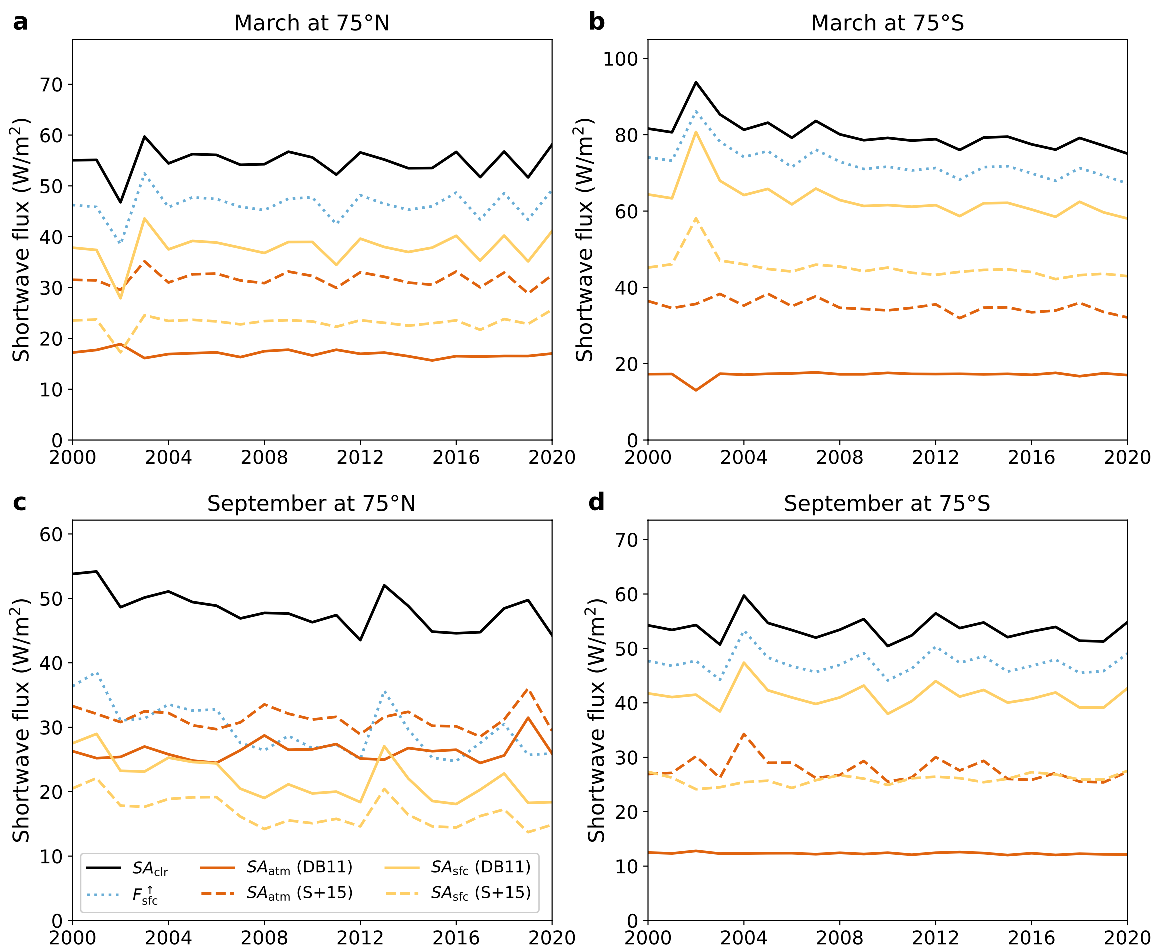

Figure S3. Zonally-averaged clear-sky shortwave fluxes at the poles during spring and fall and their atmosphere/surface decomposition under different sets of equations. TOA reflection (solid black line) and upwelling shortwave radiation at the surface (blue dotted line) are from the CERES EBAF product. Atmospheric (orange) and surface (yellow) components of the TOA reflection are calculated following either the equations of DB11 (solid colored lines) or S+15 (dashed colored lines).

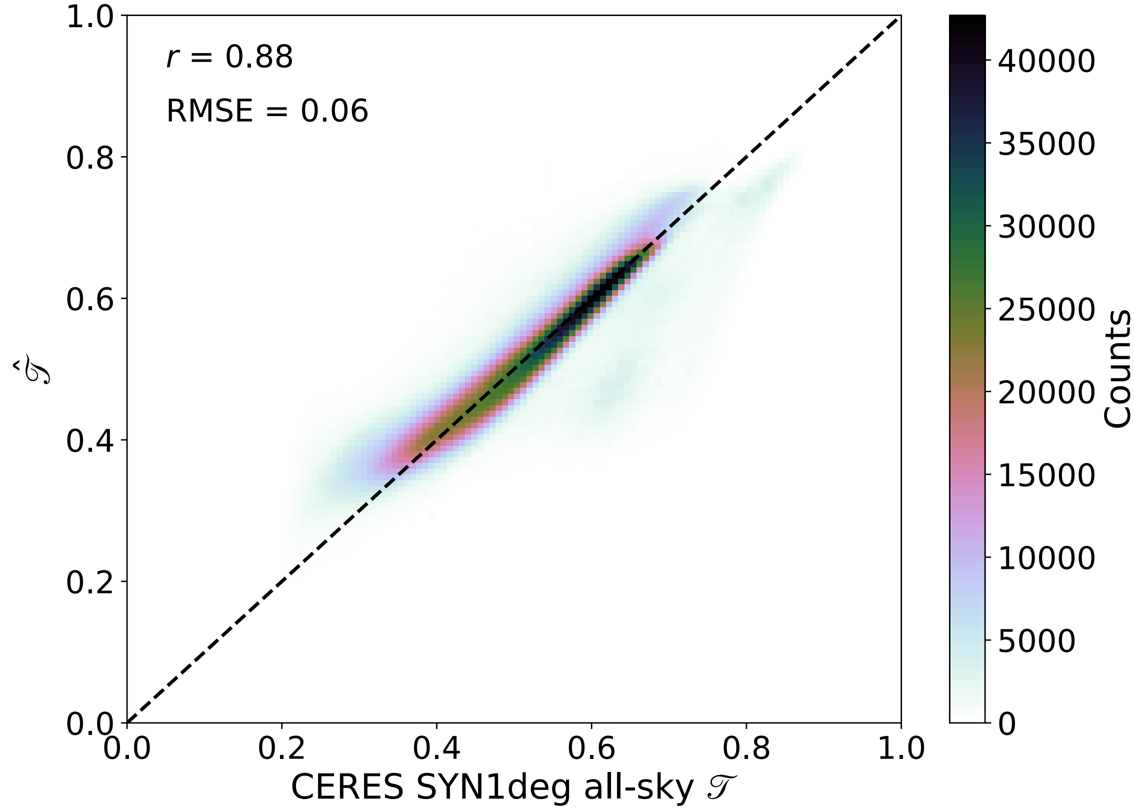

Figure S4. Correspondence between the regressed transmissivity and the CERES SYN1deg all-sky computed transmissivity. Shading represents counts in a 2D histogram with bin widths of 0.01. The dashed line represents a 1:1 relationship for reference. The Pearson's correlation coefficient (*r*) and root mean square error (RMSE) are provided in the upper-left corner.

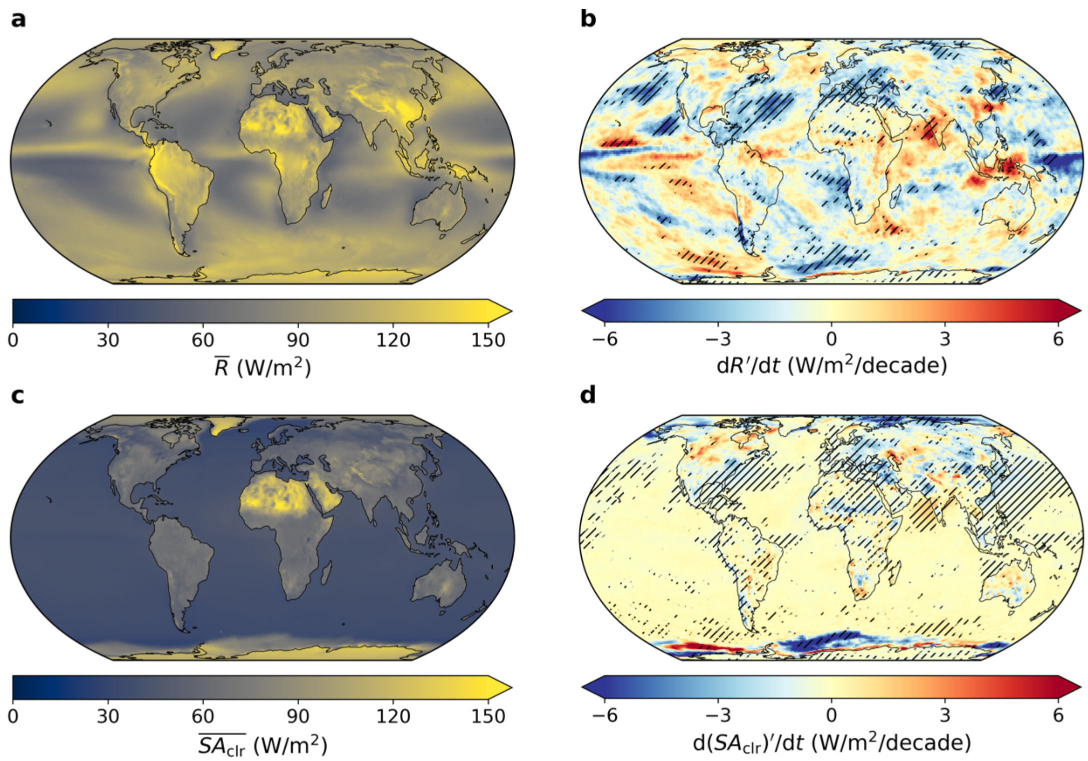

Figure S5. Maps of climatological values and trends for total all-sky and clear-sky reflection. Stippling indicates trends that are distinguishable from zero at 95% confidence in (b) and (d).

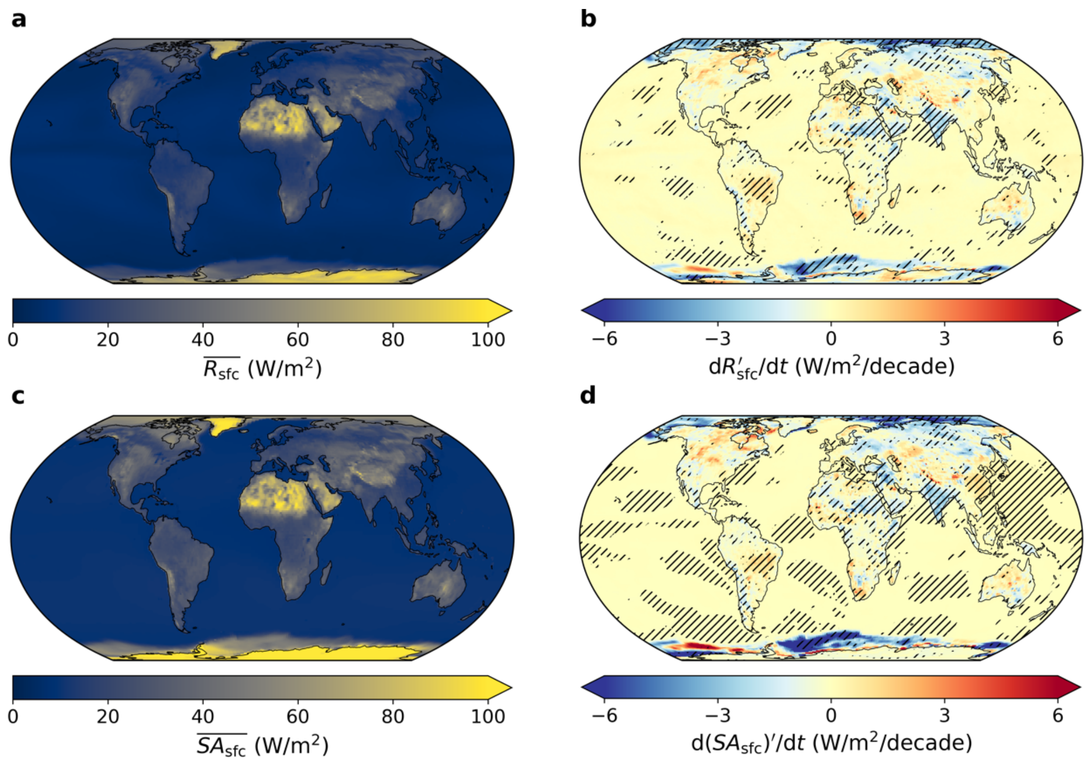

Figure S6. Maps of climatological values and trends for the surface contribution to total all-sky and clear-sky reflection. Stippling indicates trends that are distinguishable from zero at 95% confidence in (b) and (d).

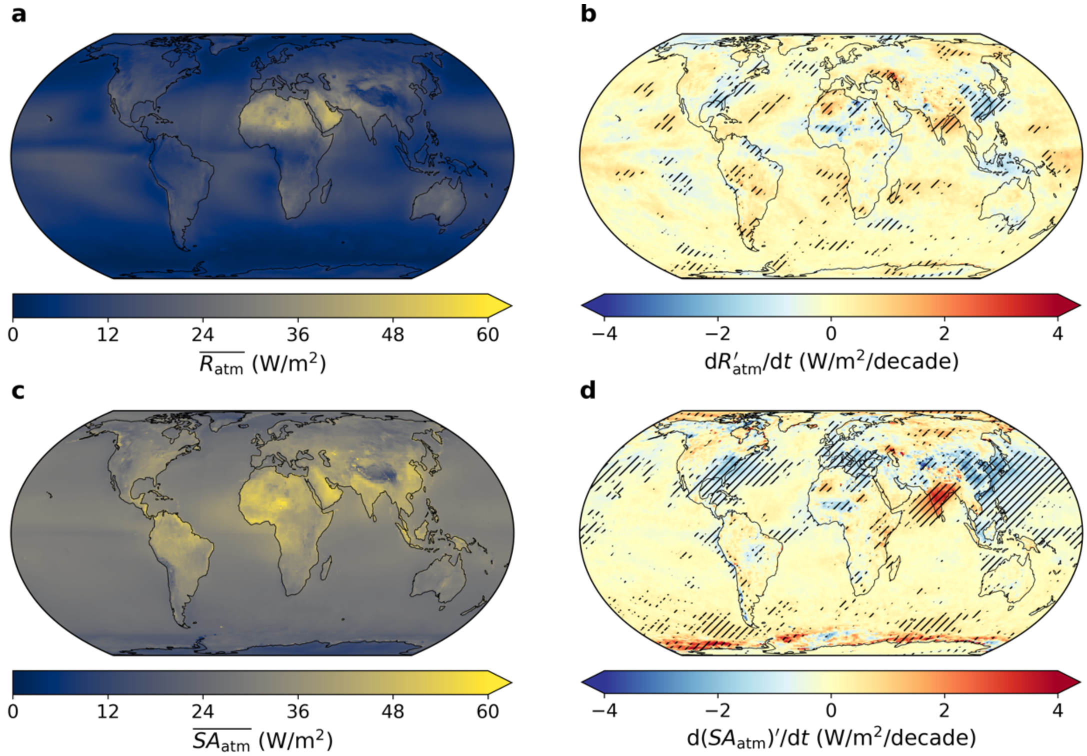

Figure S7. Maps of climatological values and trends for the atmospheric contribution to total all-sky and clear-sky reflection. Stippling indicates trends that are distinguishable from zero at 95% confidence in (b) and (d).

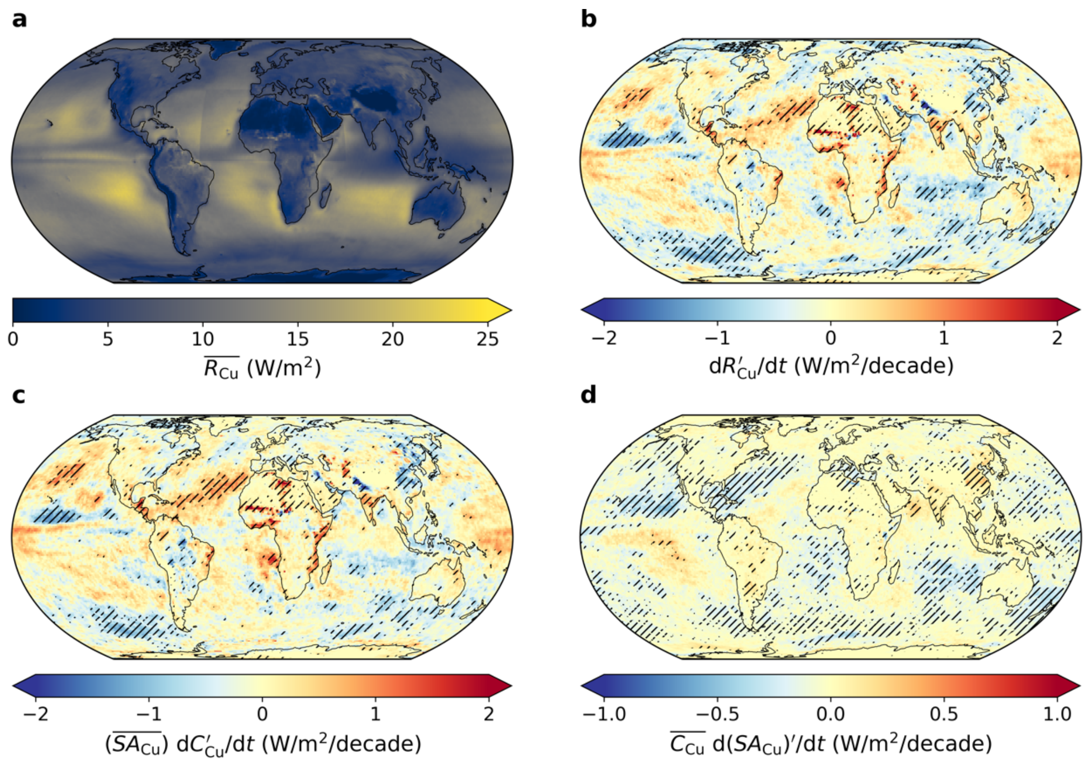

Figure S8. Maps of climatological values, total trends, and the cloud fraction and cloud albedo contributions to the total trends for cumulus cloud reflection. Stippling indicates trends that are distinguishable from zero at 95% confidence in (b-d).

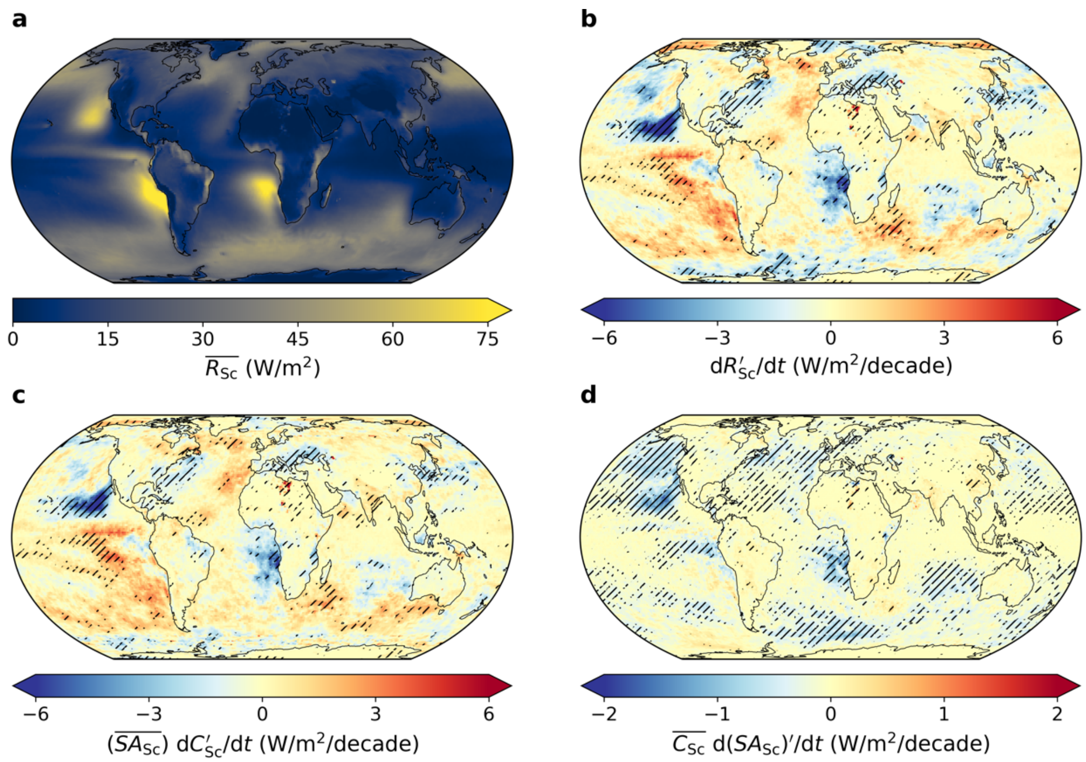

Figure S9. Maps of climatological values, total trends, and the cloud fraction and cloud albedo contributions to the total trends for stratocumulus cloud reflection. Stippling indicates trends that are distinguishable from zero at 95% confidence in (b-d).

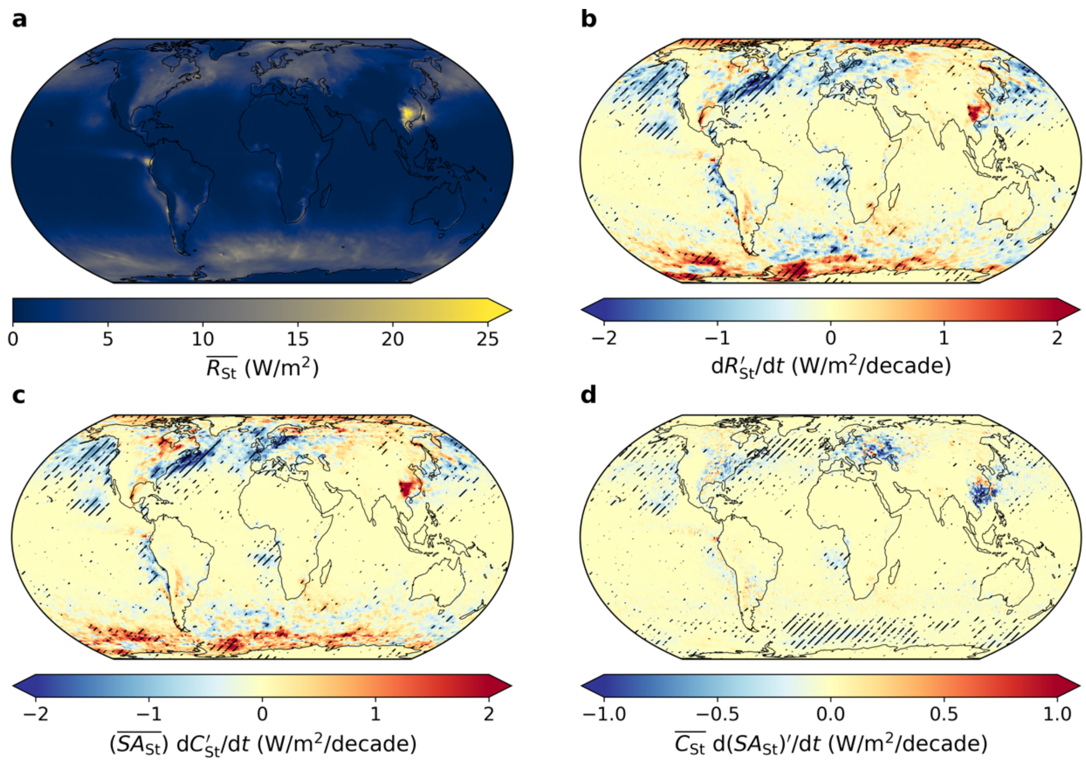

Figure S10. Maps of climatological values, total trends, and the cloud fraction and cloud albedo contributions to the total trends for stratus cloud reflection. Stippling indicates trends that are distinguishable from zero at 95% confidence in (b-d).

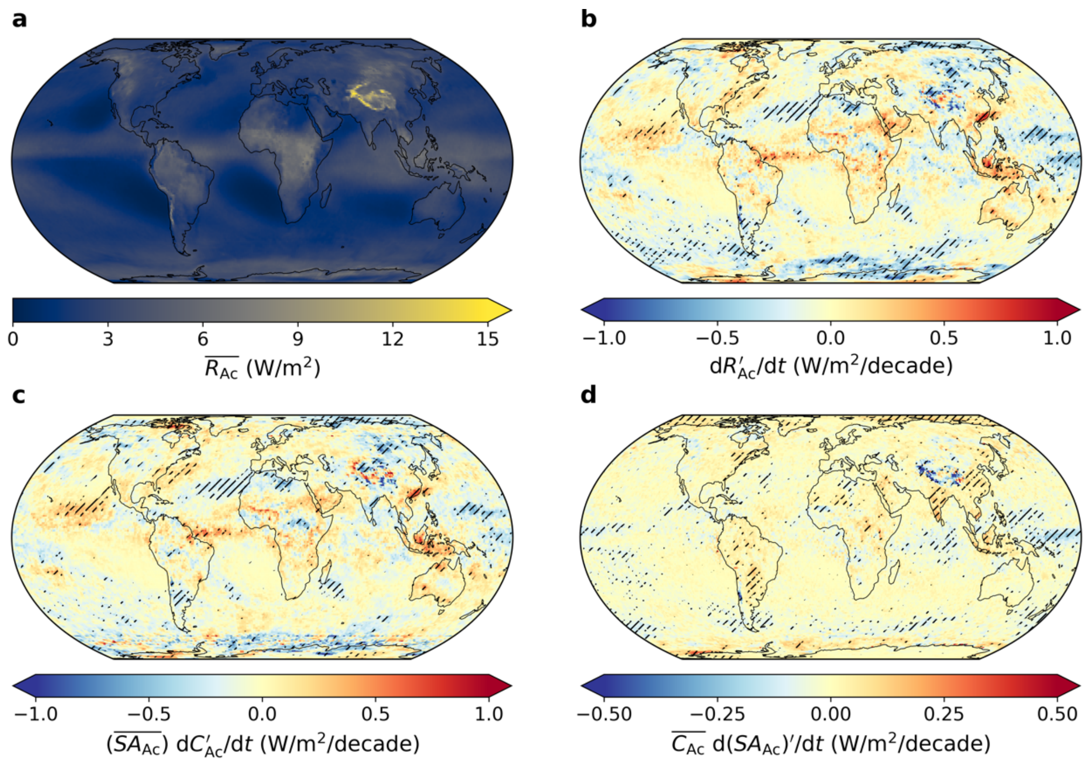

Figure S11. Maps of climatological values, total trends, and the cloud fraction and cloud albedo contributions to the total trends for altocumulus cloud reflection. Stippling indicates trends that are distinguishable from zero at 95% confidence in (b-d).

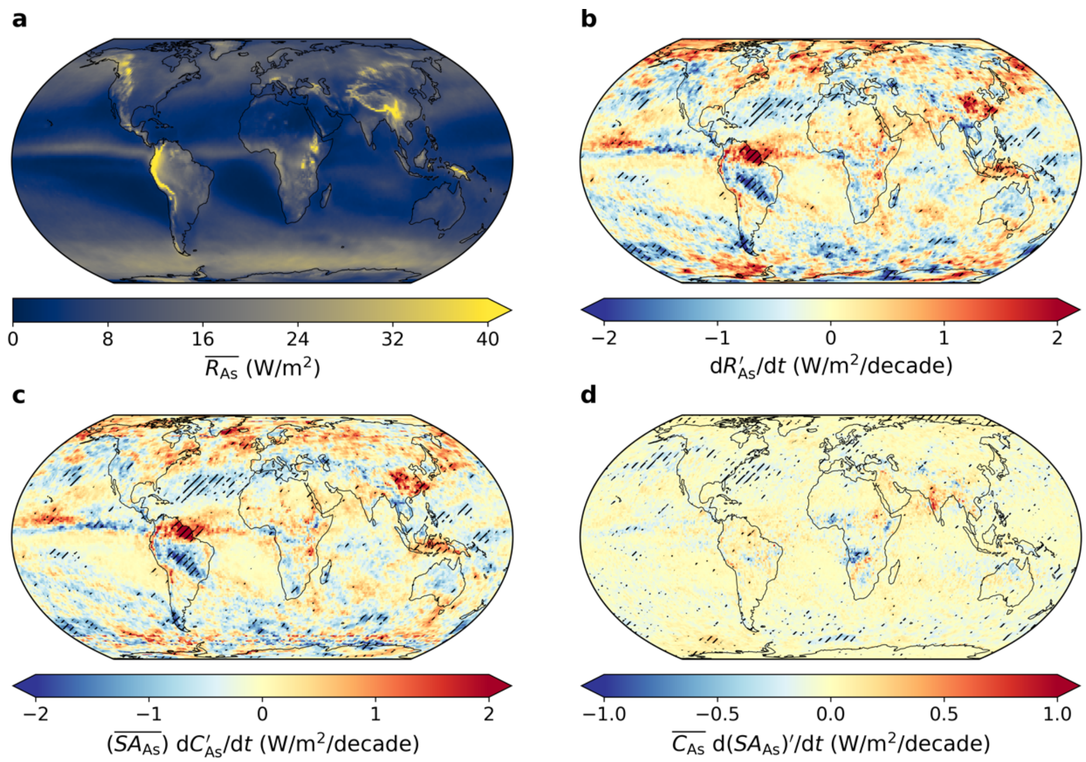

Figure S12. Maps of climatological values, total trends, and the cloud fraction and cloud albedo contributions to the total trends for altostratus cloud reflection. Stippling indicates trends that are distinguishable from zero at 95% confidence in (b-d).

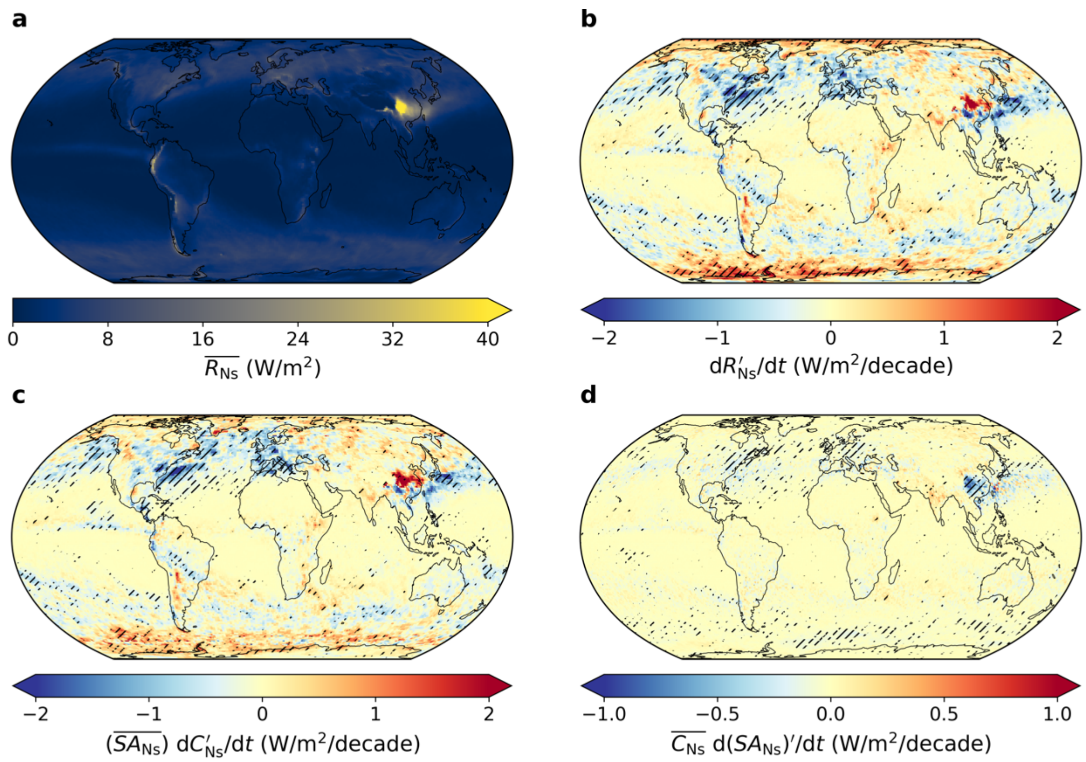

Figure S13. Maps of climatological values, total trends, and the cloud fraction and cloud albedo contributions to the total trends for nimbostratus cloud reflection. Stippling indicates trends that are distinguishable from zero at 95% confidence in (b-d).

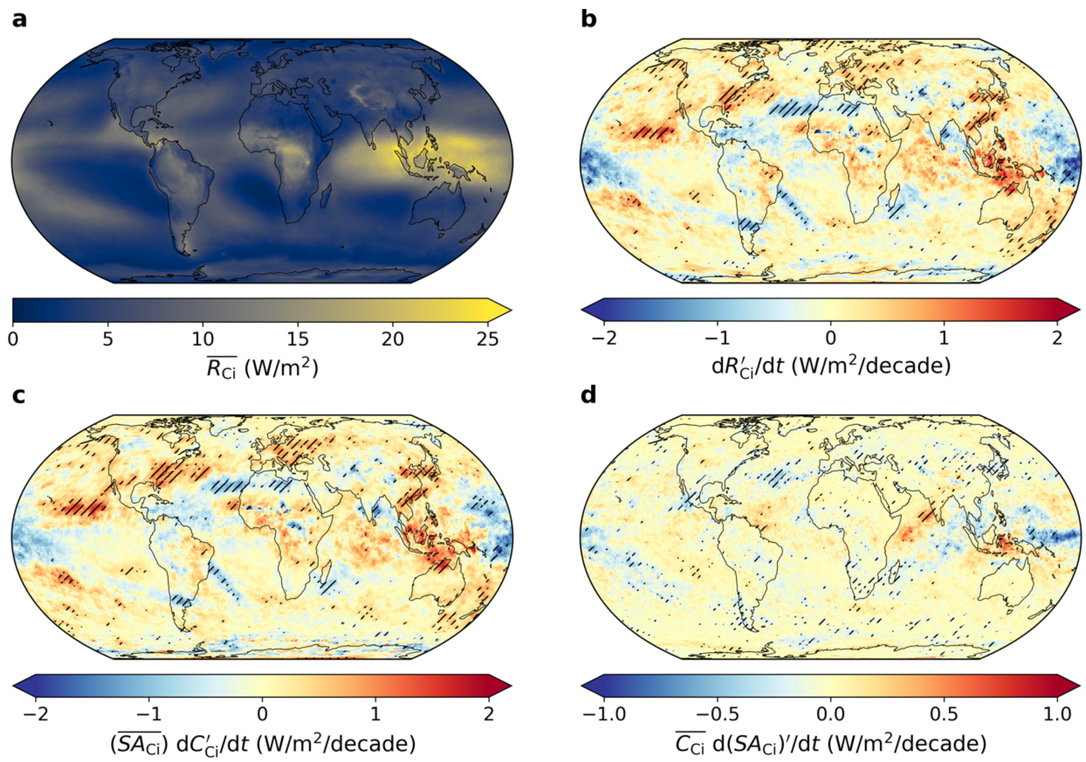

Figure S14. Maps of climatological values, total trends, and the cloud fraction and cloud albedo contributions to the total trends for cirrus cloud reflection. Stippling indicates trends that are distinguishable from zero at 95% confidence in (b-d).

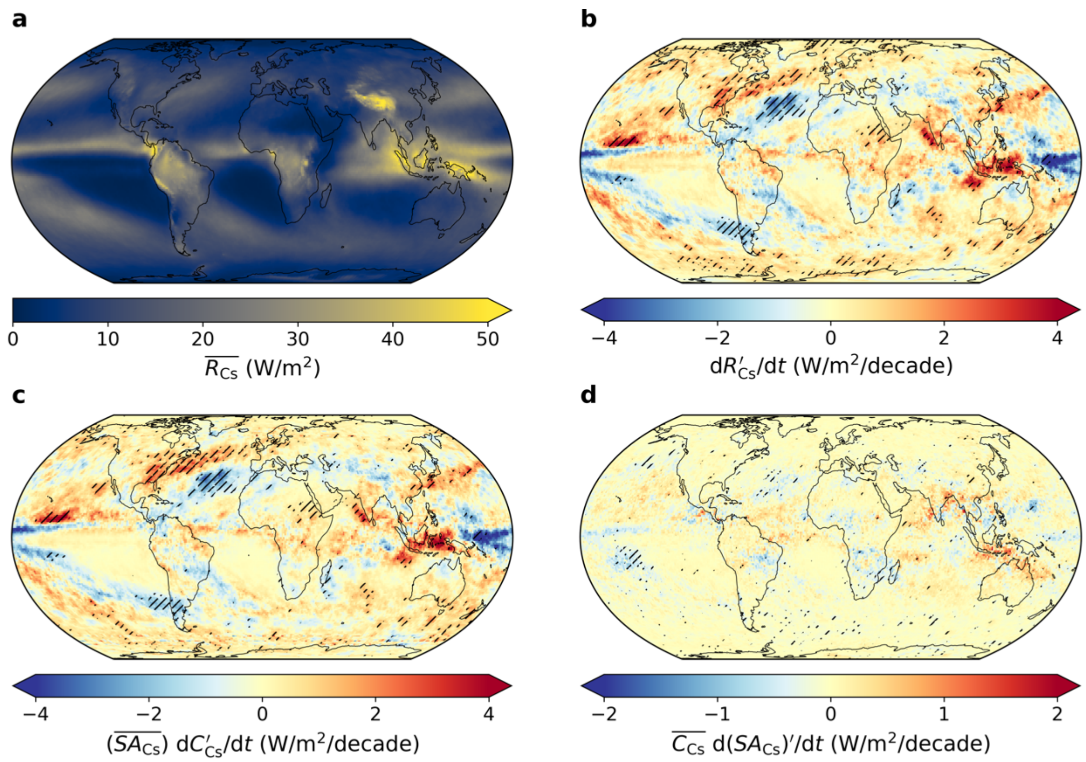

Figure S15. Maps of climatological values, total trends, and the cloud fraction and cloud albedo contributions to the total trends for cirrostratus cloud reflection. Stippling indicates trends that are distinguishable from zero at 95% confidence in (b-d).

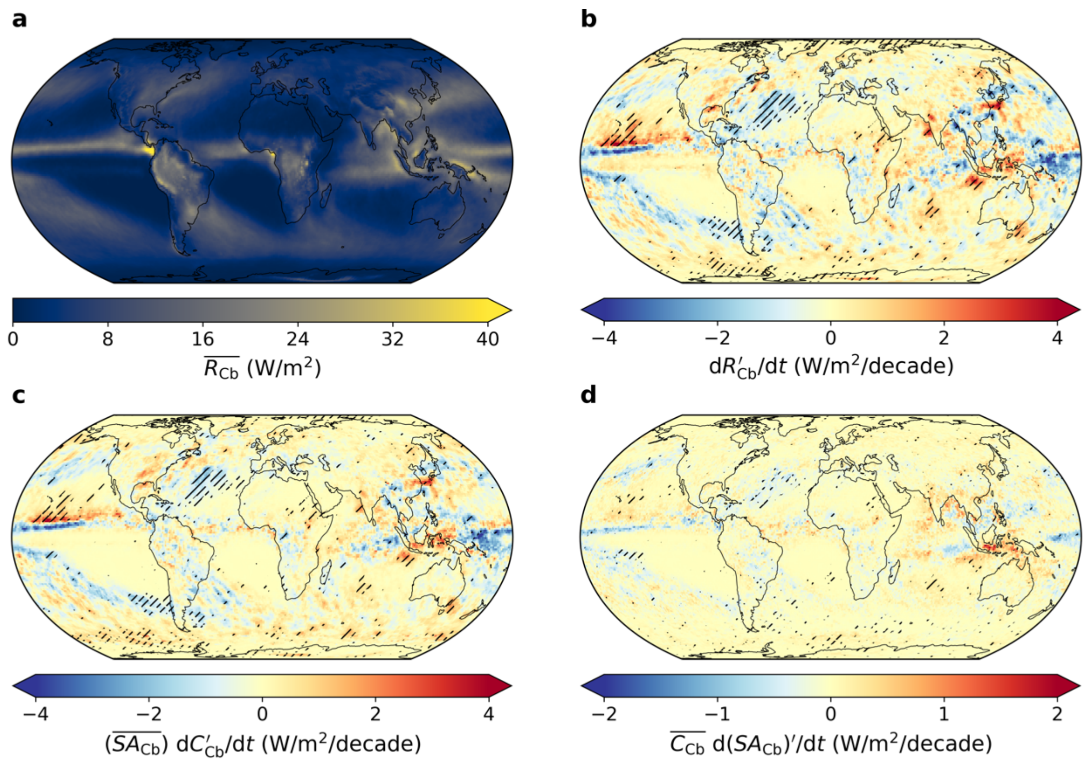

Figure S16. Maps of climatological values, total trends, and the cloud fraction and cloud albedo contributions to the total trends for cumulonimbus cloud reflection. Stippling indicates trends that are distinguishable from zero at 95% confidence in (b-d).

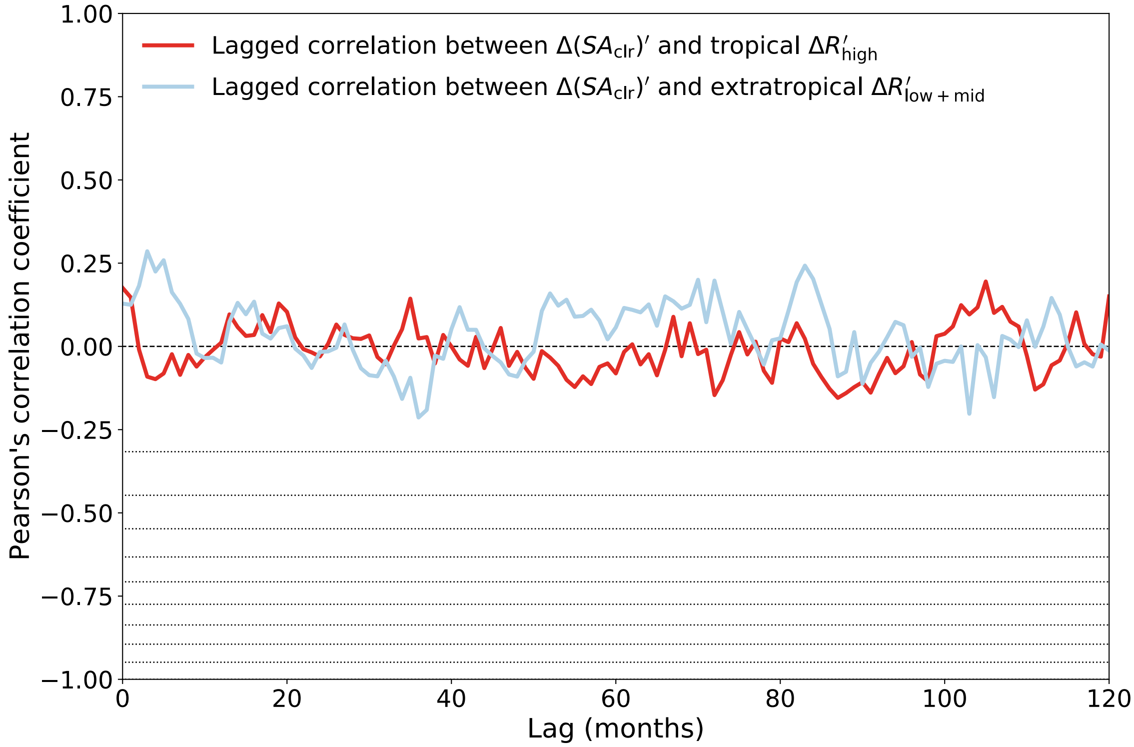

Figure S17. Lagged correlations between deseasonalized anomalies of clear-sky and tropical high cloud or extratropical low and mid cloud asymmetries. Cloud anomalies lag clear-sky anomalies. Large, negative correlations would be expected for cloud compensation of clear-sky changes. R^2 values are shown in increments of 10% via dotted lines for negative correlations only (expected sign for compensation).

	Trends (W/m^2/decade)			
	Global	**NH**	**SH**	**NH-SH**
All-sky	**-0.65 ± 0.16**	**-0.77 ± 0.23**	**-0.53 ± 0.27**	-0.24 ± 0.34
Surface	**-0.20 ± 0.08**	**-0.25 ± 0.12**	**-0.16 ± 0.15**	-0.09 ± 0.20
Clear-sky atmosphere	0.00 ± 0.05	-0.04 ± 0.08	0.05 ± 0.06	-0.08 ± 0.10
Low clouds	**-0.32 ± 0.16**	**-0.43 ± 0.19**	-0.21 ± 0.22	-0.21 ± 0.26
Cu	**-0.12 ± 0.04**	**-0.07 ± 0.05**	**-0.16 ± 0.05**	**0.10 ± 0.06**
Sc	**-0.17 ± 0.15**	**-0.26 ± 0.18**	-0.07 ± 0.21	-0.18 ± 0.25
St	**-0.04 ± 0.04**	**-0.10 ± 0.04**	0.02 ± 0.05	**-0.13 ± 0.05**
Mid clouds	**-0.19 ± 0.08**	**-0.17 ± 0.09**	**-0.22 ± 0.12**	0.05 ± 0.14
Ac	**-0.05 ± 0.02**	**-0.05 ± 0.03**	**-0.06 ± 0.03**	0.01 ± 0.04
As	**-0.09 ± 0.04**	-0.01 ± 0.06	**-0.16 ± 0.06**	**0.14 ± 0.09**
Ns	-0.05 ± 0.06	**-0.11 ± 0.06**	0.00 ± 0.10	**-0.10 ± 0.10**
High clouds	0.06 ± 0.12	0.11 ± 0.17	0.01 ± 0.17	0.09 ± 0.24
Ci	0.02 ± 0.05	0.05 ± 0.07	0.00 ± 0.06	0.05 ± 0.08
Cs	**0.13 ± 0.10**	**0.15 ± 0.14**	0.10 ± 0.15	0.05 ± 0.21
Cb	**-0.09 ± 0.05**	**-0.09 ± 0.07**	**-0.09 ± 0.06**	-0.01 ± 0.09

Table S1. Global and hemispheric trends. Errors represent 95% confidence; values in boldface are significantly different than zero.